Design and Optimization of Terahertz Waveguides with Low Loss and Dispersion

by

Vahid Shiran

B.Sc., Isfahan University of Technology, 2017

A Thesis Submitted in Partial Fulfillment of the

Requirements for the Degree of

MASTER OF APPLIED SCIENCE

in the Department of Electrical and Computer Engineering

Design and Optimization of Terahertz Waveguides with Low Loss and Dispersion

by

Vahid Shiran

B.Sc., Isfahan University of Technology, 2017

Supervisory Committee

Dr. Thomas Darcie, Supervisor

(Department of Electrical and Computer Engineering)

Dr. Jens Bornemann, Departmental Member

(Department of Electrical and Computer Engineering)

Supervisory Committee

Dr. Thomas Darcie, Supervisor

(Department of Electrical and Computer Engineering)

Dr. Jens Bornemann, Departmental Member

(Department of Electrical and Computer Engineering)

ABSTRACT

Electromagnetic waves in the terahertz (10^{12} Hz) spectral range have gained significant research focus due to their applications in various fields of science. To effectively generate and integrate terahertz waves in systems, appropriate waveguide design is critical. Conventionally waveguides have been used to control the propagation of electromagnetic waves. A waveguide with low loss and dispersion is always preferred. But achieving these characteristics is quite challenging especially if operating in the terahertz spectral range. There are inherent material and geometric limitations that exist for terahertz waveguides. It is therefore important to optimize

the design to enable their use in applications efficiently.

This thesis investigates the characteristics of three primary terahertz waveguides based on the underlying theory and results obtained from simulations. The three waveguides are parallel-plate waveguides, two-wire waveguides, and coplanar striplines. The work in this thesis mostly focuses on coplanar striplines, optimal for building a highly efficient commercial and portable terahertz system-on-chip (TSOC). The contribution of the thesis is around the use of different types of passive components mounted on a thin (1 μm) commercial Silicon Nitride membrane. A bias tee is introduced which is a combination of interdigitated electrodes and a meander inductor. The length of the interdigitated electrodes and the gap between them are 55 μm and 5 μm, respectively. The S_{21} parameter for this structure ranges from -24 dB/mm at near-zero frequencies to -0.8 dB/mm at 1 THz. This indicates that the designed bias tee can appropriately block low frequencies. Split-ring resonators are also used to act as band-stop filters. The resonant frequency of the resonator depends on the radii of the split-rings. In the optimized design, the internal radius of the outer ring is 25 μm and the external radius of the inner ring is 20 μm. This results in a narrowband band-stop filter with its resonant frequency centered at 701 GHz. The optimized final TSOC design discussed in this work uses these passive components placed on the Silicon Nitride membrane and is shown to have a total loss that is 3 dB/mm less than any of the previous work for terahertz frequencies [42].

Table of Contents

List of Figures

ACKNOWLEDGEMENTS

I would like to thank:

My supervisor Dr. Thomas Darcie, for giving me the opportunity to do terahertz devices research under his supervision and providing me with his invaluable guidance and support throughout my degree.

My lab colleagues Dr. Robert Levi Smith and Walid Gomaa, for their great help and supports.

My family, for their endless support and love.

DEDICATION

I would like to dedicate this work in memory of my mother.

Chapter 1

Introduction

This chapter defines the terahertz spectral range and its applications using terahertz radiation. An outline of various types of terahertz waveguides is presented as well. The Chapter concludes with an overview and organization of the thesis.

1.1 Terahertz and Applications

The terahertz spectral range, typically from 100 GHz to 30 THz , is located between the electronic and photonic regions (Figure (1.1)) [27]. An important advantage of terahertz frequencies is that since photon energies are low (<0.1 eV), dangers associated with ionizing radiation (>10 eV) do not exist. In addition, terahertz wavelengths are relatively short which allows them to be used for imaging with acceptable resolution [45]. The techniques of generating and detecting terahertz signals will be discussed in chapter 2 of the thesis.

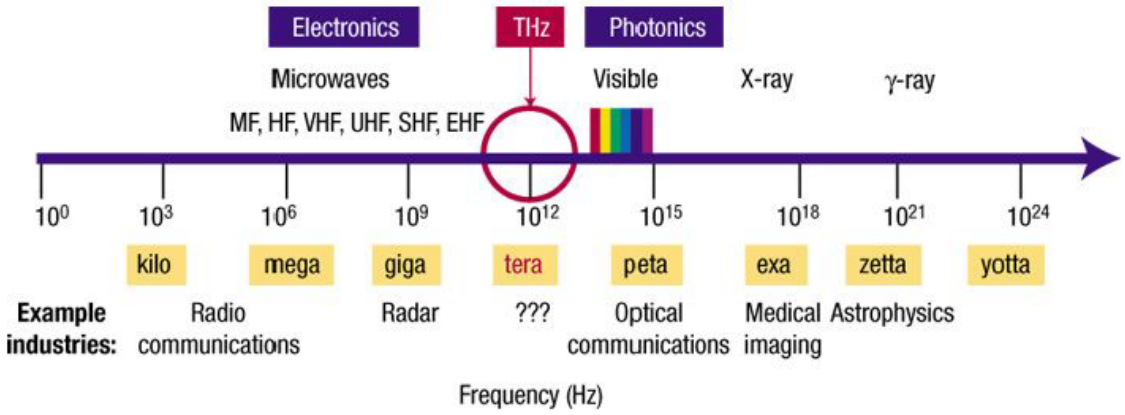

Figure 1.1: Terahertz gap. Reprinted by permission from [10]. 2002 Springer Nature

One of the main applications of terahertz radiation is using terahertz time-domain spectroscopy for the analysis of materials. The terahertz band exhibits remarkably high atmospheric opacity with the neighbouring regions of infrared radiation and radio waves. Figure (1.2) illustrates the atmospheric transmission spectrum of electromagnetic waves [28]. According to this figure, the transmittance is close to zero in the terahertz spectral range, which means that the atmosphere is absorptive in the terahertz spectral range. Water vapour in the atmosphere is particularly absorptive at terahertz frequencies, which makes the atmosphere opaque at these frequencies. Therefore, water absorption is a significant factor to be considered when outlining a scheme for a terahertz application [48].

Biological molecules have distinguishing spectral characteristics in the terahertz spectral range that are correlated with large-amplitude vibrational movements and intermolecular interactions. These molecular dynamics can be sensed by terahertz

spectroscopy. Hence, this method can be used for the detection of bombs and checking medical products and protein conformation [28].

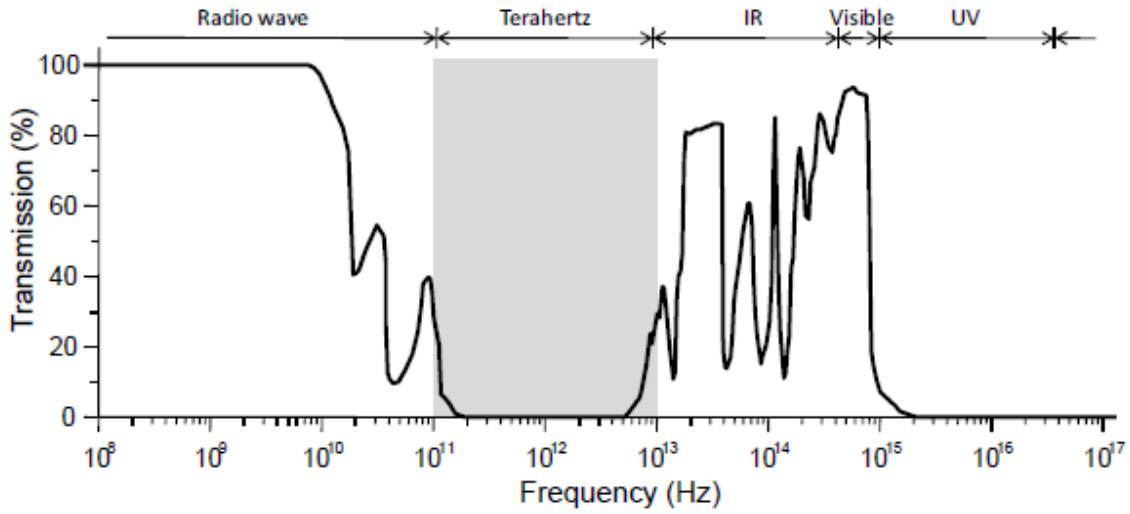

Figure 1.2: Atmospheric transmission spectrum of electromagnetic waves. Reprinted by permission from [28]. 2009 Springer

Condensed materials are generally divided into three types at terahertz frequencies with respect to their optical characteristics: water, metal and dielectric. Water is strongly absorptive at terahertz frequencies; metals are highly reflective in the terahertz spectral range due to their high electrical conductivities; dielectrics like plastics, paper and clothes are transparent at terahertz frequencies although they are typically opaque at optical frequencies [18].

The variation in material responses to terahertz enables its use in critical imaging applications. Terahertz is used to inspect sealed packaging materials as they are usually made from dielectrics. Water is absorptive at terahertz frequencies and therefore can be used to separate hydrated materials from dried objects. Metals have high

reflectivity and perfect opacity for terahertz radiation. Hence, terahertz imaging can be used to recognize weapons and explosives hidden inside legal materials [28]. The high absorption of water to terahertz radiation is beneficial for medical applications since small variations in water content can show critical weakness [53].

One of the other applications that gains significant interest, is terahertz system-on-chip. It can enable an innovative type of active terahertz electromagnetics. Terahertz wavelengths are smaller than chip dimensions. Therefore, this provides radiating and scattering surfaces in a substrate, which supports numerous high-frequency transistors as well as the capability to generate, process and sense terahertz signals simultaneously [41]. The ability to integrate and sense terahertz fields with circuits initiates a new design method for terahertz electronics. Terahertz systems emerging from this method are portable, reconfigurable and multifunctional and they are extremely encouraging because they can simultaneously provide energy-efficient ultrafast signal processing in transistors with the terahertz operation [40].

1.2 Terahertz Waveguides

To efficiently generate and integrate terahertz waves in systems-on-chip, proper waveguide design is required. Terahertz waveguides are divided into two categories: dielectric and non-dielectric. Terahertz radiation generated by photoconductive devices confined in a medium with no dielectric falls under the first category. The well-known

examples for this type are parallel-plate waveguides, and two-wire waveguides [31]. In the second category of terahertz waveguides, terahertz radiation is confined in a dielectric [11]. On-chip waveguides are examples of the second category. The on-chip waveguides usually have more attenuation and dispersion compared with waveguides that have no dielectric since the propagating electric field is mainly confined to lossy dielectric materials [5]. However, they can be fabricated as system-on-chip, that enable portability, crucial for many terahertz system applications. Lithography is the commonly used technique to fabricate terahertz system-on-chip (TSOC) which allows compact, industrialized chips containing passive components like filters [4]. Therefore, many researchers focus on the latter category of terahertz waveguides to minimize losses and dispersion.

1.3 Thesis Summary

The thesis aims to introduce the basic principles behind terahertz radiation and terahertz waveguides as well as discuss the results and the contributions of the author's work in improving the coplanar stripline design for TSOC applications. A brief overview of the chapters is given below.

Chapter 2 explains fundamental concepts in terahertz technology and terahertz time-domain spectroscopy. The chapter presents two methods to generate and detect terahertz signals using photoconductive devices.

Chapter 3 shows prior work on terahertz waveguides and transmission lines. Principles of parallel-plate and two-wire waveguides are presented. These waveguides confine terahertz radiation in free space. The attenuation characteristics and the phase constant are illustrated. Coplanar striplines, where the terahertz radiation is confined near the surface, are studied. Also, the attenuation characteristics, such as dielectric loss, radiation loss and conductor loss, are presented.

Chapter 4 presents the technique using tapered lines and the design optimization to increase the distance between two gold plates that decreases conductor losses. The chapter introduces terahertz passive components on a coplanar stripline to build a TSOC.

Chapter 5 summarizes contributions of this thesis to the field and provides a conclusion.

Chapter 2

Terahertz Generation and Detection

This chapter discusses two methods of generating and detecting terahertz signals using photoconductive devices that directly drive terahertz waveguides. Broadband terahertz pulses are generated using femtosecond laser pulses. Moreover, continuous terahertz waves are generated by mixing two laser beams with different frequencies which produces an optical beat. Eventually, the theories about terahertz pulse propagation are also discussed in this chapter.

2.1 Role of Photoconductive Devices

Terahertz fields are generated by using various techniques, such as photoconductive switching [51], photoconductive mixing [21], optical rectification [50], microwave frequency multiplication [43], backward-wave oscillators [52], free-electron lasers [6], or quantum cascade lasers [16]. These techniques of generating terahertz have advantages and disadvantages. Depending on the method, the price ranges from thousands of dollars, for the photoconductive methods, to millions of dollars, for free-electron lasers [45]. This thesis reviews terahertz generation and detection using photoconductive structures since they are less expensive than other methods of generating terahertz. Also, photoconductive devices can function at room temperature while generating and detecting radiation within a large bandwidth (more than 4 THz) and producing measurable output power.

A femtosecond laser is used to excite a photoconductive device to generate terahertz. The photoconductive device is connected to DC-voltage lines to drive the circuit. The DC-voltage creates a DC electric field which causes acceleration of photoinduced electrons in the photoconductive material. The resultant carrier density changes the material's conductivity generating a photocurrent with frequency components that can extend into the terahertz spectral range. A commercially available photoconductive substrate material is a Low Temperature Grown Gallium Arsenide (LTG-GaAs) ($E_g^{GaAs} = 1.42$ eV) semiconductor. LTG-GaAs is selected as the sub-

strate material because it can generate short duration terahertz pulses because of the rapid rise of the photo-induced current in the semiconductor and the short carrier lifetime [7].

In the receiver section, terahertz detection is quite challenging because the signal to be measured has usually a very low power. Since the spectral power density of a terahertz pulse decreases as frequency increases, the frequency spectrum of the terahertz pulse has a higher power than the noise equivalent power in lower frequencies. Therefore, it is possible to detect the terahertz pulses with frequency components less than 4 THz. After this cut-off, the noise equivalent power has magnitude comparable to the desired signal and becomes impossible to measure the signal power spectrum [22].

Heterodyne detection used in terahertz time-domain spectroscopy can remarkably enhance the signal-to-noise ratio at the receiver compared with other methods used to detect terahertz waves such as thermal detection [28]. In heterodyne detection methods, the same photoconductive device is used as a receiver. Terahertz waves are incident on the receiver and create a pulsed voltage across the gap of the photoconductive device. This voltage can be probed by measuring the receiver current when a femtosecond optical pulse excites free carriers between the gap of the photoconductive device [32].

2.2 Photoconductive Mixing

Photomixing, also called optical heterodyne downconversion, is a method to generate Continuous-Wave (CW) terahertz radiation with a photoconductive mixer. LTG-GaAs is a common photoconductive material for this method since it has high mobility and short lifetime. The tuning range of the photoconductive mixer can be surprisingly broad provided a high-quality, tunable, dual-frequency laser system is obtainable. The basic drawback of this technique is that the output power is relatively low compared with other techniques of CW terahertz generation. Its optical-to-terahertz conversion efficiency is $10^{-6} - 10^{-5}$, and the typical output power is in the microwatt range. Since photomixing needs continuous optical excitation, the low thermal conductivity of LT-GaAs ($\sim 15\ W/mK$) limits the maximum terahertz output power [2, 28].

The optical excitation in photomixing uses a beat between two CW laser beams with finely tuned disparate frequencies. CW terahertz is generated by mixing two lasers, v_1 and v_2, which have a nanometer-scale difference in their wavelengths, $\Delta\lambda$. The mixed beam is incident onto the photoconductive device. The best mixing takes place when the spatial distribution and polarization state of the two lasers are exactly the same. Eq. (2.1) describes the beat frequency for a typical photomixer where c is the speed of light in a vacuum. For example, to obtain a beat frequency of $1.265\ THz$ at a center wavelength of $\lambda_c = 854\ nm$, a wavelength separation of $\Delta\lambda = 2.431\ nm$ is needed [44].

$$f_{beat} = \Delta v = \frac{c\Delta\lambda}{(\lambda_c - \frac{\Delta\lambda}{2})(\lambda_c + \frac{\Delta\lambda}{2})} \tag{2.1}$$

For two beams with powers P_1 and P_2 , and frequencies v_1 and v_2, the incident optical power incident on the semiconductor is given by [14]:

$$P(\omega, t) = P_1 + P_2 + 2\sqrt{mP_1P_2}cos(\omega t) \tag{2.2}$$

where $\omega = 2\pi(v_1 - v_2)$, and m is a parameter to denote the quality of the spatial overlap between the two lasers and varies between 0 (no overlap) to 1 (completely matched).

The carrier density in the photoconductive gap can be expressed by:

$$\frac{dn}{dt} = \frac{\eta}{hvAd}P(\omega, t) - \frac{n}{\tau} \tag{2.3}$$

where η is the quantum efficiency, n is the photocarrier density, d is the absorption depth, A is the active area, hv_c is the photon energy, and $\omega = 2\pi\Delta v$

The method of terahertz generation using photomixing is achieved by driving a photoconductor device with oscillating optical pump intensity. This is obtained by applying a constant voltage across a modulated conductor and is described by [44]:

$$G(\omega, t) \approx \frac{\mu ed\sqrt{A}}{r}n(\omega, t) \approx G_0[1 + \beta sin(\omega t + \phi)] \tag{2.4}$$

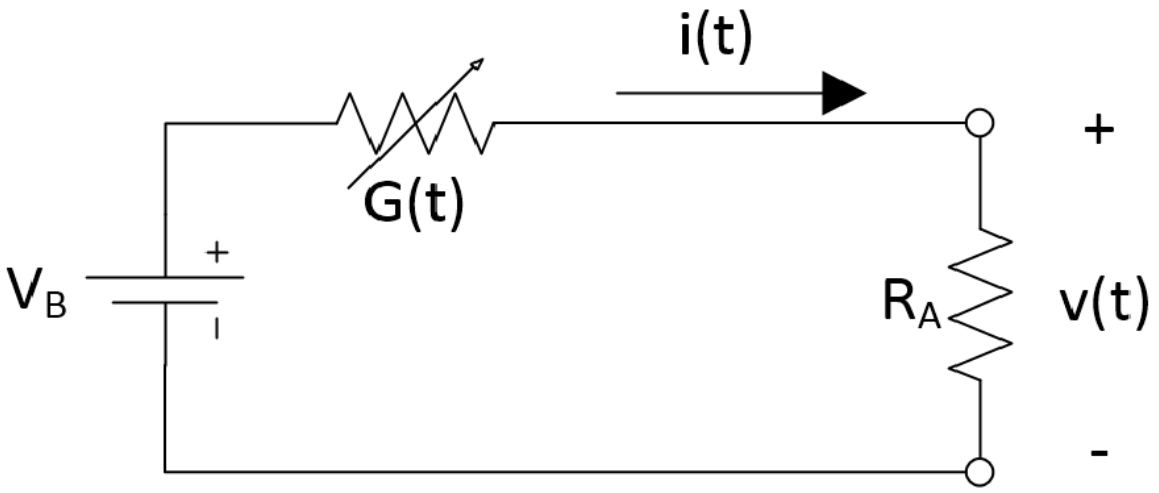

Figure 2.1: The equivalent circuit of a photomixer

where μ is the effective carrier mobility, e is the elementary charge, r is the width of the photoconductive gap. The second part of Eq. (2.4) is derived to enable an easy understanding of photomixing; G_0 is the average photoconductance and β denotes the modulation of the photoconductor.

The efficiency of photomixing is not high because of the average source resistance, $\frac{1}{G_0} \cong 1\ M\Omega$, which is much larger than the input impedance of the waveguide driven by the photomixing device. As a result, this large difference between them restricts functionality of the photomixing device.

This concept is depicted in Figure (2.1) which represents an ideal photomixer (without any capacitance). The relative equations for the current and voltage are given by [44]:

$$i(t) = \frac{G(t)V_B}{G(t)R_A + 1}, \tag{2.5}$$

$$v(t) = i(t)R_A = \frac{G(t)V_B R_A}{G(t)R_A + 1} \tag{2.6}$$

and the total radiated power is described by:

$$P_{rad} = (\frac{i_{p-p}}{2\sqrt{2}})^2 R_A \tag{2.7}$$

where i_{p-p} is the peak to peak current and the amount of radiated power is around tens of nanowatts.

There is another issue that causes a decrease in the received power. This arises from the substrate's response time being too large at terahertz frequencies. In other words, if the substrate's carrier lifetime is longer than the terahertz period, the terahertz power will decrease. Therefore, this issue limits the efficiency of the photomixer devices.

2.3 Generation of Terahertz Pulses with Biased Photoconductive Devices

Subpicosecond terahertz pulses can be generated from a biased photoconductive device excited by femtosecond laser pulses [28]. When the femtosecond pulse hits the photoconductive device, it generates photocarriers and they accelerate along the direction of the DC-electric field created by DC-voltage towards the metal electrodes.

The emitted terahertz field is given by [28]:

$$E_{THz}(t) = \frac{\mu_0 l}{4\pi} \frac{sin\theta}{r} \frac{d}{dt_r} [I_{PC}(t_r)]\hat{\theta} \propto \frac{dI_{PC}(t)}{dt}, \tag{2.8}$$

where l is the spot size of the optical beam, I_{PC} is the photocurrent in the gap of the photoconductive device, r is the distance from the active area, θ is the azimuth of the generated terahertz pulse transferred through the waveguide and μ_0 is the vacuum permeability ($4\pi \times 10^{-7}\ H/m$). The terahertz electric field is proportional to the time derivative of the photocurrent in the gap of the photoconductive device.

The conductance is also a function of the incident optical power for photoconductive switching, similar to photomixing. The instantaneous peak pulse power is approximately 4 kW for photoswitching while the maximum power is tens of milliwatts for photomixing. The range of the conductance for a photoconductive switch and the radiation resistance, for the duration of time the laser is incident, becomes similar and causes more current to be driven through the antenna. As a result, the terahertz output power will increase [44].

2.4 Detection of Terahertz Pulses with Photoconductive Devices

In contrast to transmitters, there is no applied biasing voltage for receivers. The incident terahertz field provides the bias voltage across the gap of the photoconductive device at the receiver. The terahertz field does drive a measurable photocurrent in the circuit. Once a photocurrent is generated, a lock-in amplifier is used to detect the current and electronics come into play to ready the signal for a computer to process the data [24]. In other words, the terahertz electric field induces a current in the photoconductive gap when the photocarriers are injected by the optical probe pulse. The photocurrent lasts for the carrier lifetime, which should be much shorter than the terahertz pulse duration for a time-resolved waveform measurement. The induced photocurrent is proportional to the field amplitude of the terahertz radiation focused on the photoconductive gap. The terahertz pulse shape is mapped out in the time-domain by measuring the current while varying the time delay between the terahertz pulse and the optical probe. Since the photocurrent signal is too weak, we should enhance the signal-to-noise ratio by a lock-in amplifier which is synchronized with an optical intensity modulator like an optical chopper [28]. This photocurrent can be calculated by:

$$J(t) = \int_{-\infty}^{t} \sigma_s(t - t') E_{THz}(t') dt' \tag{2.9}$$

where $\sigma_s(t)$ is the receiver surface conductivity and $E_{THz}(t)$ is the incident terahertz pulse. $\sigma_s(t)$ is given by:

$$\sigma_s(t) = \frac{2\sigma_0}{\sqrt{\pi}\tau_p} \int_{-\infty}^{t} e^{-t'^2/\tau_p^2}[1 - e^{-(t-t')/\tau_s}]e^{-(t-t')/\tau_c}dt' \tag{2.10}$$

where τ_c is the carrier lifetime, τ_s is the momentum relaxation time, and σ_0 is given by:

$$\sigma_0 = \frac{\sqrt{\pi}e\mu_e(1 - R_{opt})I_0\tau_p}{2\hbar\omega} \tag{2.11}$$

where e is the electron charge, μ_e is the receiver's electron mobility, R_{opt} is the substrate reflectance, I_0 is the optical intensity, $\hbar = \frac{h}{2\pi}$ where h is Planck's constant, ω is the angular frequency, τ_p is the optical pulse width, τ_s is the momentum relaxation time, and τ_c is the carrier lifetime.

2.5 Pulse Propagation

Electromagnetic pulse propagation is important while considering TSOCs. Several factors affect pulse propagation. However, waveguide geometry and material characteristics have a greater influence than other factors. Electric field propagation in the frequency domain is given by :

$$\hat{E}_{out}(\omega) = e^{-jk(\omega)z}\hat{E}_{in}(\omega) \tag{2.12}$$

where $\hat{E}_{out}(\omega)$ and $\hat{E}_{in}(\omega)$ are the Fourier transforms of the input and output pulses, respectively, ω is the angular frequency, z is the propagation distance, and $k(\omega)$ is the wavenumber.

Complexities associated with field propagation arise from the fact that $k(\omega) = \beta(\omega) - j\alpha(\omega)$, where $\alpha(\omega)$ is the attenuation constant and $\beta(\omega)$ is the phase constant. For a plane wave in a lossless vacuum system $\alpha(\omega) = 0$ and $\beta(\omega) = \omega/c$, where c is the speed of light. Considering the above relationships, the output electric filed is represented as:

$$\hat{E}_{out}(\omega) = e^{-j\omega z/c}\hat{E}_{in}(\omega) \tag{2.13}$$

Eq. (2.13) indicates that the output is a time-shifted product of the input, which is a great simplification to apply to numerous utilizations. This scenario is not plausible throughout the whole electromagnetic spectrum because of the realistic material characteristics. In the non-ideal plane wave scenario that either the permittivity or permeability of the propagation medium is dependant on frequency, the phase constant is provided by:

$$\beta(\omega) = \omega\sqrt{\epsilon(\omega)\mu(\omega)} \tag{2.14}$$

where $\epsilon(\omega) = \epsilon_0\epsilon_r(\omega)$ is the complex permittivity and $\mu(\omega) = \mu_0\mu_r(\omega)$ is the complex permeability. The vacuum permittivity (ϵ_0) is equal to $8.8542 \times 10^{-12}\ F/m$ and the vacuum permeability (μ_0) is equal to $4\pi \times 10^{-7}\ H/m$. Since $\epsilon(\omega)$ and $\mu(\omega)$

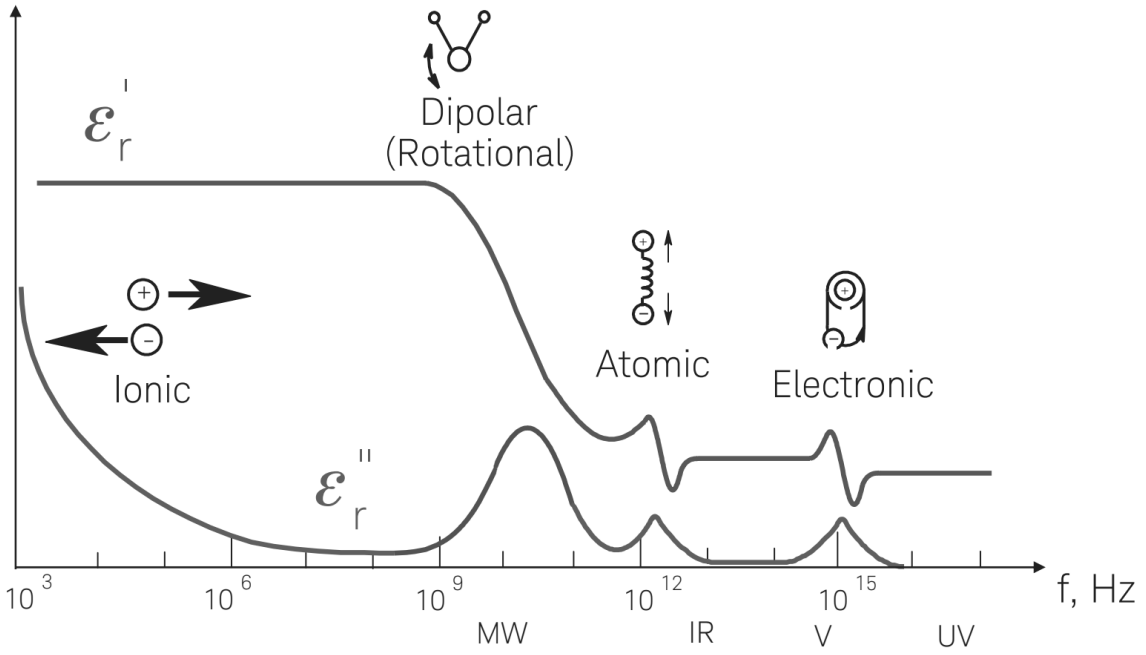

Figure 2.2: Frequency response of dielectric mechanisms [25]

depend on the frequency, Eq. (2.13) should be adjusted such that the output is no longer a simple time shift of the input. When ignoring magnetic materials, $\mu_r = 1$. In this condition, Figure (2.2) demonstrates a total form of $\epsilon_r(\omega) = \epsilon_r'(\omega) - j\epsilon_r''(\omega)$ of the electromagnetic spectrum , with the same scale of ϵ' and ϵ'', from Direct Current (DC) to the Ultra Violet (UV) range. It is apparent from Figure (2.2) that the dielectric function becomes more complex above 1 GHz.

2.5.1 Attenuation

Attenuation takes place through many mechanisms. Mostly, imperfect dielectrics (such as Silicone Nitride) and conductors (such as gold) have attenuation, say α_d and α_c respectively. When attenuation is considered as an imaginary part of $k(\omega)$, Eq.

(2.12) is modified, and the propagating wave is provided by:

$$\hat{E}_{out}(\omega) = e^{-j\beta(\omega)z} e^{-\alpha(\omega)z} \hat{E}_{in}(\omega) \tag{2.15}$$

which implies that there is attenuation in the output electric field when $\alpha(\omega) > 0$. The total attenuation coefficient, $\alpha(\omega) = \alpha_d(\omega) + \alpha_c(\omega)$, is provided in Nepers (Nps) per unit length and indicates a decrease in the field amplitude by $1/e$ over that length [45].

The attenuation coefficient for a particular structure is computed from the power loss per unit length, P_l, which is given by [35]:

$$P(z) = P_0 e^{-2\alpha z} \tag{2.16}$$

where P_0 is the input power. As a result:

$$P_l(z) = -\frac{\partial P(z)}{\partial z} = 2\alpha P_0 e^{-2\alpha z} = 2\alpha P(z) \quad \rightarrow \quad \alpha = \frac{P_l(z=0)}{2P_0} \tag{2.17}$$

As mentioned before, α arises due to the conductor and dielectric attenuation.

Dielectric loss

The imaginary part of the dielectric function, $\epsilon(\omega) = \epsilon'(\omega) - j\epsilon''(\omega)$, represents dielectric loss. It is typical to designate the dielectric loss tangent, $tan\delta_\epsilon = \epsilon''(\omega)/\epsilon'(\omega)$,

to the dielectric loss. By applying this designation, the dielectric function can be represented in terms of the loss tangent:

$$\epsilon(\omega) = \epsilon'(\omega)[1 - jtan\delta_\epsilon(\omega)] = \epsilon_0\epsilon(\omega)[1 - jtan\delta_\epsilon(\omega)] \tag{2.18}$$

Transverse electric ($\bar{E}$) and magnetic field ($\bar{H}$) attributes need to be known to determine the dielectric attenuation coefficient for a particular guiding structure. The input power, P_0, should be determined initially by integrating the Poynting vector:

$$P_0 = \frac{1}{2}Re\int_S \bar{E} \times \bar{H}^*.d\bar{s} \tag{2.19}$$

and the dielectric power loss and attenuation coefficient per unit length are provided by [35]:

$$P_{ld} = \frac{\omega\epsilon''(\omega)}{2}\int_V |\bar{E}|^2 ds, \quad \rightarrow \quad \alpha_d = \frac{P_{ld}}{2P_0} \tag{2.20}$$

where the integration takes place in the transverse plane ($\hat{x}$,$\hat{y}$) over the dielectric region and up to a unit length in the propagation direction ($\hat{z}$). The dielectric attenuation coefficient is ordinarily denoted by:

$$\alpha_d(\omega) \propto \omega\epsilon''(\omega)Z_0(\omega) \tag{2.21}$$

where $Z_0(\omega)$ is the characteristic impedance of the particular guiding structure.

Conductor loss

Conductor loss relates to the attenuation correlated with field propagation throughout a conductor with finite conductivity. A principal factor in calculating the conductor loss is the surface resistance, R_s. Since high-frequency waves cannot propagate into a conductor deeply, surface resistance becomes important. The penetration depth is determined by skin depth. Skin depth is a depth inside the surface of a conductor at which the current density decreases with the rate of $1/e$=0.37. It is given by [35]:

$$\delta_s = \sqrt{\frac{2}{\omega\mu(\omega)\sigma}} \tag{2.22}$$

where σ is the conductivity of the metal. After calculating the skin depth, the surface resistance is given by [35]:

$$R_s(\omega) = \frac{1}{\sigma\delta_s(\omega)} \tag{2.23}$$

With a similar way to find the dielectric attenuation coefficient, Eq. (2.20), the conductor attenuation coefficient can be determined [35]:

$$P_{lc} = \frac{R_s(\omega)}{2}\int_S |\bar{H}_t|^2 ds, \quad \rightarrow \quad \alpha_c = \frac{P_{lc}}{2P_0} \tag{2.24}$$

where the integration takes place in the transverse plane ($\hat{x}$,$\hat{y}$) over the conduc-

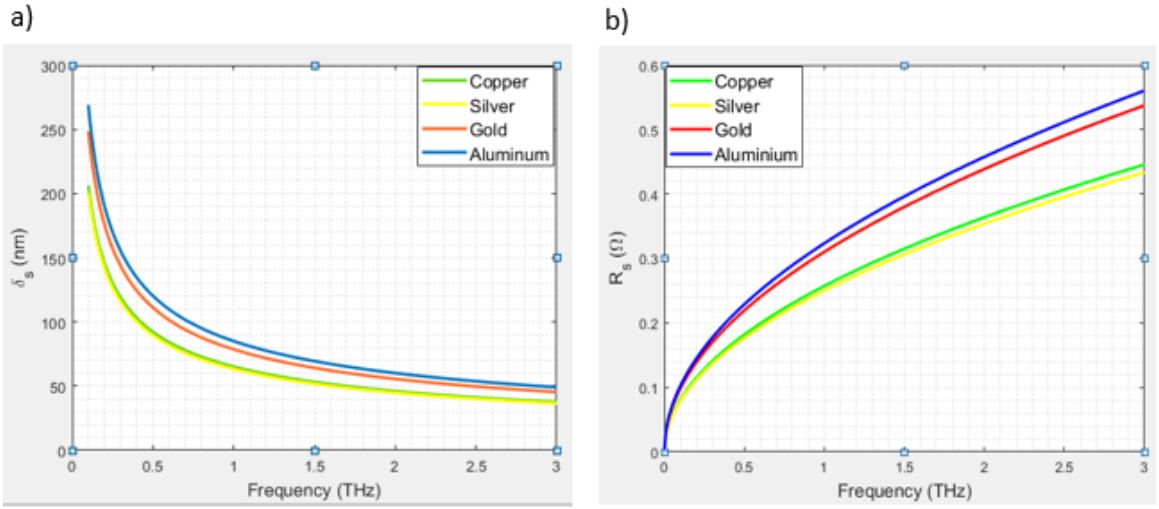

Figure 2.3: a.) Skin depth and b.) Surface resistance in the terahertz region for a few useful metals.

tor surface, while $\hat{z}$ is the propagation direction. Also, The conductor attenuation coefficient usually has the following form:

$$\alpha_c(\omega) \propto \frac{R_s(\omega)}{Z_0(\omega)} \tag{2.25}$$

Figure (2.3) shows a comparison between the skin depth and surface resistance for four metals at terahertz frequencies. It is worth mentioning that $R_s(\omega) \propto \sqrt{\omega}$ according to the figure; thus, the conductor loss will enhance with this rate of frequency dependence. Although gold does not have the lowest surface resistance among other metals, it is used as a conductor in terahertz waveguides due to its durability. It is the most corrosion-proof and oxidation-resistant metal [37].

Chapter 3

Terahertz Waveguides

In the previous chapter, photoconductive devices were introduced and their properties were investigated. The work discussed in this thesis focuses not on photoconductive antennas that radiate terahertz but rather on photoconductive devices that directly drive transmission lines while suppressing radiation. This chapter details the previous work on terahertz waveguides and introduces the principles behind parallel-plate waveguides, two-wire waveguides and coplanar striplines.

A waveguide is a device used to transfer electromagnetic waves in a system without substantial loss. A common type of waveguide for radio waves and microwaves is a hollow metal pipe [8]. Optical fibers are also utilized in the optical frequency spectrum as waveguides. Fiber-optic communication uses the low dispersion and attenuation of silica-based optical fibers for transferring light with wavelength in the range 1.3-1.6 μm. Many microwave (metallic) and optical (dielectric) waveguide technologies have

been tested in the terahertz region. The main challenge for waveguide technologies in this frequency spectrum is the relatively high absorption in most of the conventional waveguide materials [28].

3.1 Previous Work on TSOCs

Previous work on broadband TSOCs using coplanar striplines can be broadly classified into two types. These works discuss the design and fabrication of these waveguides alongside the challenges that need to be overcome. The first type of waveguides have high losses and considerable dispersion due to the existence of radiation and dielectric losses from using a thick dielectric. Passive components such as filters have been designed and mounted in this design [5], [4]. The second category is a novel terahertz coplanar stripline, fabricated on a thin (1 μm) Silicon Nitride membrane to eliminate the radiation and dielectric losses [42]. This waveguide has less losses and dispersion than the former but had less than optimal conductor losses. Furthermore, use of passive components in the design had not been considered or discussed.

3.2 Transmission Line Theory

Fundamental transmission line theory needs to be understood to identify ways of minimizing the losses and dispersion occurring with terahertz waveguides. Transmission line theory investigates complex power transfer between a source and load, while

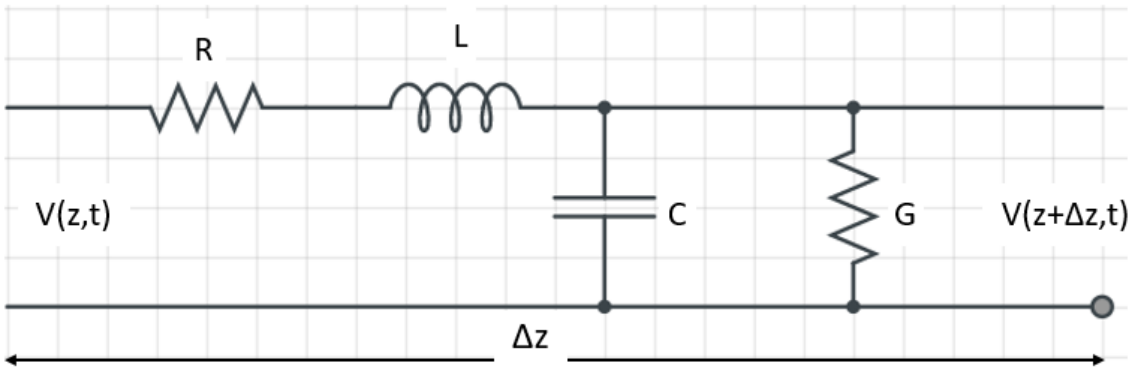

Figure 3.1: Equivalent circuit of an infinitesimal slice of a transmission line with a length of ΔZ

a transmission line is a fraction of a wavelength in size [35]. The complex power transfer occurs when voltages and currents can change in magnitude and phase over the length of the transmission line. According to Figure (3.1), each infinitesimal slice (Δz) of transmission line has four main components: a series resistor per unit length (R), a series inductor per unit length (L), a parallel capacitor per unit length (C) and a parallel conductor per unit length (G).

To investigate losses and dispersion of a transmission line, the complex propagation constant (γ) should be calculated, which depends on the components of the infinitesimal slice of a transmission line. It is given by [35]:

$$\gamma = \alpha + j\beta = \sqrt{(R + j\omega L)(G + j\omega C)} \tag{3.1}$$

where α is the attenuation constant, per unit distance, and β is the phase constant, per unit length, of the transmission line. Losses can be analyzed from the attenuation

constant and dispersion can be determined by the phase constant. This method will be used in the next sections to analyze losses and dispersion of terahertz waveguides.

Transverse electromagnetic (TEM) waves have field configurations where neither the electric nor the magnetic field components ($E_z = H_z = 0$) exist in the propagation direction. Transverse electric (TE) waves are characterized by the fact that the electric field is transverse to the direction of propagation, while the magnetic field is not. Transverse magnetic (TM) waves are characterized by the fact that the magnetic field is transverse to the direction of propagation, while the electric field is not. Both TM and TE modes are not ideal for broadband terahertz because they have dispersive characteristics. Broadband terahertz signals can propagate without dispersion with a TEM guided mode in a dispersionless medium [44].

According to Maxwell's equations, we have [35]:

$$\nabla \times \vec{E} = -j\omega\mu\vec{H} \tag{3.2}$$

$$\nabla \times \vec{H} = j\omega\epsilon\vec{E} \tag{3.3}$$

$$\frac{\partial E_z}{\partial y} + j\beta E_y = -j\omega\mu H_x \tag{3.4}$$

$$-j\beta E_x - \frac{\partial E_z}{\partial x} = -j\omega\mu H_y \tag{3.5}$$

$$\frac{\partial E_y}{\partial x} - \frac{\partial E_x}{\partial y} = -j\omega\mu H_z \tag{3.6}$$

$$\frac{\partial H_z}{\partial y} + j\beta H_y = j\omega\epsilon E_x \tag{3.7}$$

$$-j\beta H_x - \frac{\partial H_z}{\partial x} = j\omega\epsilon E_y \tag{3.8}$$

$$\frac{\partial H_y}{\partial x} - \frac{\partial H_x}{\partial y} = j\omega\epsilon E_z \tag{3.9}$$

As stated in the last paragraph, a TEM wave has no axial field components. Hence, the above equations can be simplified for a TEM mode:

$$\beta E_y = -\omega\mu H_x \tag{3.10}$$

$$\beta E_x = \omega\mu H_y \tag{3.11}$$

$$\frac{\partial E_y}{\partial x} = \frac{\partial E_x}{\partial y} \tag{3.12}$$

$$\beta H_y = \omega\epsilon E_x \tag{3.13}$$

$$-\beta H_x = \omega\epsilon E_y \tag{3.14}$$

$$\frac{\partial H_y}{\partial x} = \frac{\partial H_x}{\partial y} \tag{3.15}$$

We can return to Eq. (3.10) and Eq. (3.14) and eliminate H_x to find β:

$$\begin{aligned} \beta^2 &= \omega^2\mu\epsilon E_y \\ \beta &= \omega\sqrt{\mu} = k \end{aligned} \tag{3.16}$$

where k is the wavenumber of the material used for the transmission line. Therefore, the phase constant is equal to the wavenumber for TEM modes. After that, we reach Helmholtz wave equations by taking the curl of Eq. (3.2) and Eq. (3.3):

$$\nabla^2 \vec{E} + \omega^2 \mu \epsilon \vec{E} = \nabla^2 \vec{E} + k^2 \vec{E} = 0 \tag{3.17}$$

$$\nabla^2 \vec{H} + \omega^2 \mu \epsilon \vec{H} = \nabla^2 \vec{H} + k^2 \vec{H} = 0 \tag{3.18}$$

For e^{-jkz} dependance, Eq. (3.17) and Eq. (3.18) reduce to equations consisting only transverse fields:

$$\nabla_t^2 \vec{e_t}(x, y) = 0 \tag{3.19}$$

$$\nabla_t^2 \vec{h_t}(x, y) = 0 \tag{3.20}$$

If we imagine that there is no longitudinal field component, $e_z = 0$ and $h_z = 0$, we can express transverse fields as an electrostatic field:

$$\vec{e_t}(x, y) = -\nabla_t \Phi(x, y) \tag{3.21}$$

$$-\nabla_t^2 \Phi(x, y) = 0 \tag{3.22}$$

For a TEM mode propagation, two conductors are needed since a voltage has to exist in the transverse plane. However, TE and TM waveguide modes do not have this limitation (two conductors) [35], [44].

3.3 Methods to Analyze Microwave Networks

In microwave engineering, any N-port network can be described with different matrices, such as impedance [Z] or admittance matrix [Y], transmission (ABCD) matrix, and scattering matrix [S]. This thesis only studies scattering and transmission matrices since simulation and theoretical results are only expressed by these matrices.

3.3.1 The Scattering Matrix

The scattering matrix can give us complete information about the network. The scattering matrix is relevant to the voltage waves incident on the ports and reflected voltage waves from the ports. The scattering parameters can be computed with network analysis techniques for some passive elements and microwave circuits. Apart from that, the scattering parameters can be measured directly with a network analyzer [35].

For a two-port network like Figure (3.2), V_n^+ $(n = 1, 2)$ is considered as the amplitude of the voltage wave incident on port n, and V_n^- is the amplitude of the voltage wave reflected from port n. Therefore, the scattering matrix is described below:

$$\begin{bmatrix} V_1^- \\ V_2^- \end{bmatrix} = \begin{bmatrix} S_{11} & S_{12} \\ S_{21} & S_{22} \end{bmatrix} \begin{bmatrix} V_1^+ \\ V_2^+ \end{bmatrix} \tag{3.23}$$

For a N-port network, a single element of the scattering matrix ($[S]$) can be found

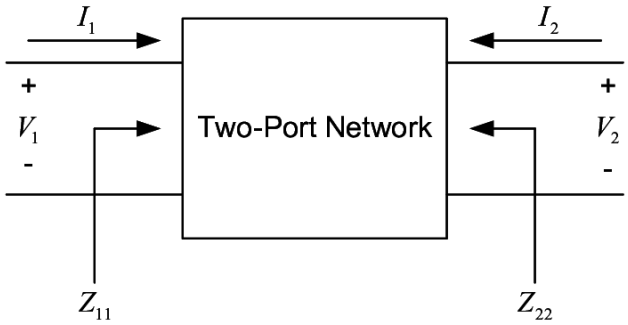

Figure 3.2: A two-port network

by:

$$S_{ij} = \left.\frac{V_i^+}{V_j^+}\right|_{V_k^+=0 \ for \ k\neq j} \tag{3.24}$$

From Eq. (3.24) it is evident that S_{ij} can be calculated by exciting port j with an incident wave of voltage V_j^+, and measuring the amplitude of the reflected wave, V_i^-, going out from port i. There should not be any incident wave on any port except the jth port, which indicates that all ports should be terminated in match loads to not have reflections. Hence, S_{ii} is defined as the reflection coefficient when all ports except port i are terminated in matched loads, and S_{ij} is the transmission coefficient from port j to port i when all other ports are terminated in matched loads.

If the N-port network is reciprocal and lossless, we can have known equations between scattering matrix elements making the analysis of the network easier. One of those equations is given by [35]:

$$\sum_{k=1}^{N} S_{ki} S_{kj}^* = \delta_{ij}, \tag{3.25}$$

where $\delta_{ij} = 1$ if $i = j$ and $\delta_{ij} = 0$ if $i \neq j$ is the Kronecker symbol. Hence, if $i = j$ Eq. (3.25)is simplified to:

$$\sum_{k=1}^{N} S_{ki} S_{kj}^{*} = 1, \tag{3.26}$$

Otherwise, if $i \neq j$ Eq. (3.25) is simplified to:

$$\sum_{k=1}^{N} S_{ki} S_{kj}^{*} = 0, \tag{3.27}$$

Eq. (3.26) indicates that the dot product of any column of the scattering matrix with the conjugate of that column equals to one (unity). However, Eq. (3.27) shows that the dot product of any column with the conjugate of a different column equals to zero (orthogonal).

To have a perfect two-port waveguide, S_{11} and S_{22} should be close to zero. Also, S_{12} and S_{21} have to be near one. It means that that waveguide has small reflection loss and most of the wave can transfer from one port to the other port.

S-parameter magnitudes are shown in one of two methods, linear magnitude or logarithmic based decibels (dB). The formula for decibels is given by:

$$S_{ij}(dB) = 20log(S_{ij}(magnitude)) \tag{3.28}$$

It is noticeable that power ratios are expressed as 10 $log(magnitude)$ while Voltage ratios are 20 $log(magnitude)$ since power is proportional to voltage squared.

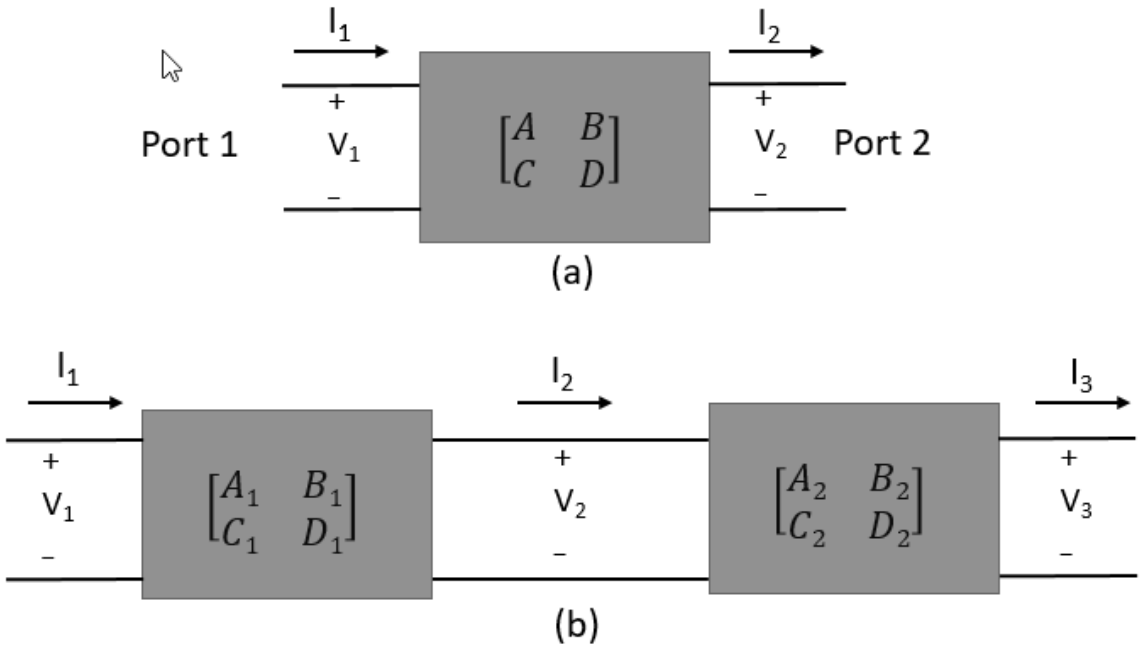

Figure 3.3: a) A two-port network, b) A cascade connection of two-port networks

3.3.2 The Transmission (ABCD) Matrix

The [Z], [Y], and [S] matrices can describe a microwave network with an arbitrary number of ports. However, in reality, many microwave networks consist of a cascaded combination of two-port networks. For each two-port network, it is beneficial to establish a 2×2 transmission (ABCD matrix). Subsequently, it will be shown that if we obtain the ABCD matrix for individual two-port elements in a cascaded configuration of two-port networks and multiply them respectively, thus, we can find the total ABCD matrix of the entire network [35].

The ABCD matrix for a network illustrated in Figure (3.3a), in terms of the total

voltages and currents, is represented as:

$$\begin{aligned} V_1 &= AV_2 + BI_2, \\ I1 &= CV_2 + DI_2, \end{aligned} \tag{3.29}$$

or as a matrix form:

$$\begin{bmatrix} V_1 \\ I_1 \end{bmatrix} = \begin{bmatrix} A & B \\ C & D \end{bmatrix} \begin{bmatrix} V_2 \\ I_2 \end{bmatrix} \tag{3.30}$$

Figure (3.3b) illustrates the cascaded connection of two-port networks, the related equations are given by:

$$\begin{bmatrix} V_1 \\ I_1 \end{bmatrix} = \begin{bmatrix} A_1 & B_1 \\ C_1 & D_1 \end{bmatrix} \begin{bmatrix} V_2 \\ I_2 \end{bmatrix} \tag{3.31}$$

$$\begin{bmatrix} V_2 \\ I_2 \end{bmatrix} = \begin{bmatrix} A_2 & B_2 \\ C_2 & D_2 \end{bmatrix} \begin{bmatrix} V_3 \\ I_3 \end{bmatrix} \tag{3.32}$$

$$\begin{bmatrix} V_1 \\ I_1 \end{bmatrix} = \begin{bmatrix} A_1 & B_1 \\ C_1 & D_1 \end{bmatrix} \begin{bmatrix} A_2 & B_2 \\ C_2 & D_2 \end{bmatrix} \begin{bmatrix} V_3 \\ I_3 \end{bmatrix} \tag{3.33}$$

The above matrix relationships imply that the multiplication of the ABCD matrices for individual two-port networks is equal to the total ABCD matrix of the cascaded connection of the two networks. It is noteworthy to learn that the order of multiplication of the matrix has to be identical to the order in which the networks

are designed. Due to this fact that matrix multiplication is generally not commutive.

ABCD matrix representation is significantly beneficial since a library of ABCD matrices for simple two-port networks can be built up, and utilized to find more complicated microwave networks which consist of the cascaded connection of simpler networks [35].

As an example [35], the ABCD parameters of a two-port network, (Figure (3.4)), which consist of a series impedance Z between ports 1 and 2, as per Eq. (3.30), is given by:

$$A = \left.\frac{V_1}{V_2}\right|_{I_2=0}, \tag{3.34}$$

implying that A is the ratio of $\frac{V_1}{V_2}$ when there is no current in port 2. When there is no current in port 1, V_1 is equal to V_2 since A will be equal to 1. Also, other ABCD parameters in open-circuit condition will be:

$$B = \left.\frac{V_1}{I_2}\right|_{V_2=0} = \frac{V_1}{V_1/Z} = Z \tag{3.35}$$

$$C = \left.\frac{I_1}{V_2}\right|_{I_2=0} = 0 \tag{3.36}$$

$$D = \left.\frac{I_1}{I_2}\right|_{V_2=0} = \frac{I_1}{I_1} = 1 \tag{3.37}$$

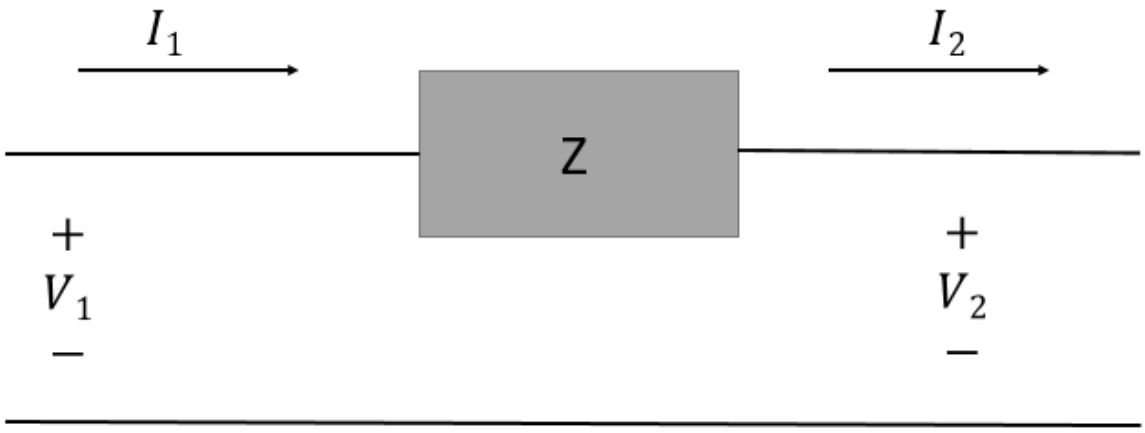

Figure 3.4: A two-port network with a series impedance Z

3.4 Existing Terahertz Waveguides

Transmission line theory and Maxwell's equations were studied in the last sections. They will be used to investigate the characteristics of three primary terahertz waveguides.

3.4.1 Parallel-Plate Waveguides

A Parallel-Plate Waveguide (PPWG) is able to support TEM waves [16]. Figure (3.5) shows a parallel-plate waveguide that consists of two thin conductive plates with height T, separation distance S, and length W.

If we ignore fringing fields and consider $T \gg S$, the electrostatic expression for a parallel-plate waveguide is gained from Laplace's equation (Eq. (3.22)). The plate's potential are given by $\Phi(x = -\frac{S}{2}, y) = -\frac{V_0}{2}$ and $\Phi(x = \frac{S}{2}, y) = \frac{V_0}{2}$, respectively.

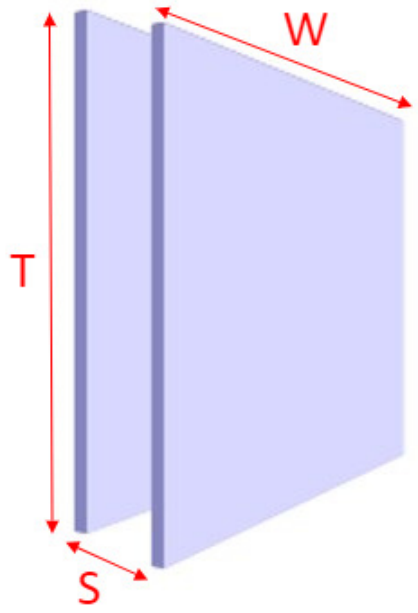

Figure 3.5: Parallel Plate Waveguide

Therefore, we can simplify Laplace's equation to:

$$\nabla_t^2 \Phi(x,y) = \left[\frac{\partial^2}{\partial x^2} + \frac{\partial^2}{\partial y^2}\right]\Phi(x,y) \tag{3.38}$$

Therefore, we will have:

$$\frac{d^2\Phi(x)}{dx^2} = 0 \tag{3.39}$$

Hence, after solving this differential equation, $\Phi(x)$ can be represented as:

$$\Phi(x) = c_1 + c_2 x \tag{3.40}$$

$$\Phi\left(x = -\frac{S}{2}\right) = c_1 + c_2\left(-\frac{S}{2}\right) = -\frac{V_0}{2} \tag{3.41}$$

$$\Phi\left(x=\frac{S}{2}\right)=c_1+c_2\left(\frac{S}{2}\right)=\frac{V_0}{2} \tag{3.42}$$

As a result, c_1 and c_2 will be 0 and $\frac{V_0}{S}$ respectively.

$$\Phi(x)=\frac{V_0 x}{S} \tag{3.43}$$

We can derive the transverse field from, Eq. (3.21) [44]:

$$\vec{e_t}(x)=-\nabla_t\Phi(x)=-\left[\hat{x}\frac{\partial}{\partial x}+\hat{y}\frac{\partial}{\partial y}\right]\frac{V_0 x}{S}=-\hat{x}\frac{V_0}{S} \tag{3.44}$$

$$\vec{h_t}(x)=\frac{1}{\eta}\hat{z}\times\vec{e_t}(x)=\hat{y}\frac{1}{\eta}\frac{V_0}{S} \tag{3.45}$$

Since TEM modes have no low-frequency cut-off, the fields are given by:

$$\vec{E}(x,y,z)=\vec{e_t}e^{-jkz}=-\hat{x}\frac{V_0}{S}e^{-jkz} \tag{3.46}$$

$$\vec{H}(x,y,z)=\vec{h_t}e^{-jkz}=-\hat{y}\frac{1}{\eta}\frac{V_0}{S}e^{-jkz} \tag{3.47}$$

If we use the transmission line model of a parallel-plate waveguide, we can find useful information about this waveguide. For a parallel-plate waveguide, the value for each transmission line component, per unit length, is given by [35]:

$$L=\frac{\mu S}{w} \tag{3.48}$$

$$C = \frac{\epsilon' w}{S} \tag{3.49}$$

$$R = \frac{2R_s}{w} \tag{3.50}$$

$$G = \frac{\omega \epsilon'' w}{S} \tag{3.51}$$

where $\mu = \mu_0 \mu_r$, ϵ' and ϵ'' are the real part and imaginary part of the permittivity, respectively, S is the separation distance between the two plates, w is the length of the plates, ω is the angular frequency and R_s is the surface resistance of the conductive material which is:

$$R_s = \sqrt{\frac{\omega \mu}{2\sigma}} \tag{3.52}$$

where σ is the conductance of the metal. Additionally, we can find the attenuation constant and phase constant of a waveguide by knowing its equivalent circuit components to calculate the waveguide's loss and dispersion:

$$\gamma = \alpha + j\beta = \sqrt{(R + j\omega L)(G + j\omega C)} \tag{3.53}$$

where γ is the complex propagation constant, α is the attenuation constant, and β is the phase constant. If we consider air ($\epsilon' = 8.85 \times 10^{-12}\ F/m$, $\epsilon'' = 0\ F/m$) as a dielectric for a parallel-plate waveguide and gold (σ_{gold}=$4 \times 10^7\ S/m$) as a material

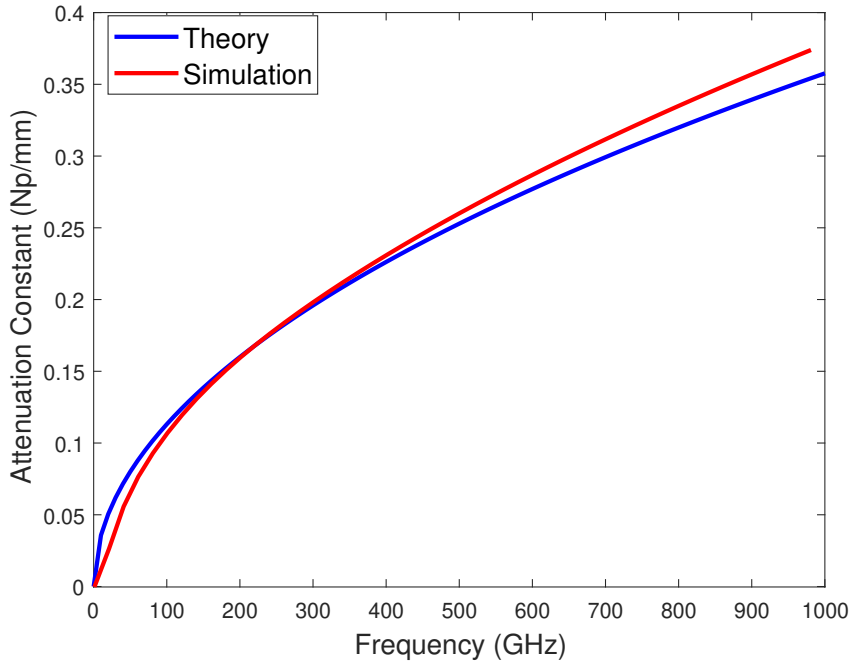

Figure 3.6: Theoretical and simulated results for parallel-plate waveguide attenuation constant with $S = 20\ \mu m$

for the plates, Eq. (3.53) is simplified to:

$$\gamma_{PPWG} = \alpha + j\beta = \sqrt{-\omega^2\mu\epsilon' + j\omega\frac{2R_s\epsilon'}{S}} \tag{3.54}$$

We can plot the real part and imaginary part of the Eq. (3.54) by MATLAB and observe the behavior of the waveguides.

The attenuation constant (real part of γ) is plotted in Figure (3.6) with $D = 20\ \mu m$. The theoretical values differ from the simulation plot due to the fringing electric field, which occurs at the edge of the plates, and limitations with mesh accuracy.

3.4.2 Two-Wire Waveguides

The main problem in designing terahertz waveguides is that many materials are extremely absorbent in the terahertz spectral range [23]. An effective waveguide design has to maximize the electromagnetic field density in the air because the lowest absorption loss takes place in the air. Metal wires are appropriate waveguides to transport terahertz pulses with low attenuation and almost no dispersion. There are generally two types of metal-wire waveguides: single-wire and two-wire waveguides. The principle mode is radially polarized in a single-wire waveguide. The coupling between a terahertz pulse and a radially-polarized mode is not easily achievable because photoconductive devices, which generate linearly polarized terahertz light, cannot be utilized directly for the sufficient excitation of this mode [30]. Therefore, two-wire waveguides are better than single-wire waveguides at terahertz frequencies since they have desirable characteristics: high coupling efficiency and low loss behaviour [31]. Furthermore, the guided mode in between the two wires has high confinement, and it reduces bending loss. Also, the group velocity dispersion and absorption losses of the guided TEM mode in a two-wire waveguide are low [30]. Therefore, in this section, the characteristics of only two-wire waveguides are explored.

We use the transmission line model of a two-wire waveguide to find its complex propagation constant, similar to the method that used for parallel-plate waveguides.

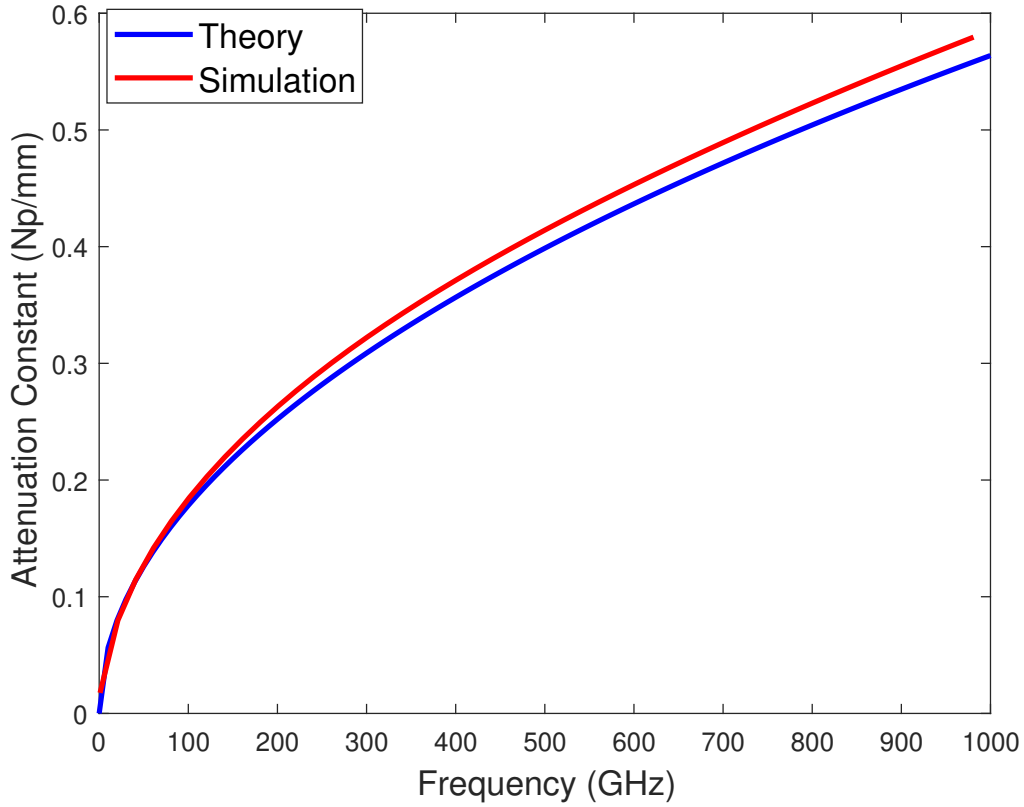

Figure 3.7: Theoretical and simulated results for two-wire waveguide attenuation constant with $D = 20\ \mu m$, and $a = 5\ \mu m$

The equivalent circuit component values for a two-wire waveguide are [35]:

$$L = \frac{\mu}{\pi} cosh^{-1}\left(\frac{D}{2a}\right) \tag{3.55}$$

$$C = \frac{\pi\epsilon'}{cosh^{-1}(D/2a)} \tag{3.56}$$

$$R = \frac{R_s}{\pi a} \tag{3.57}$$

$$G = \frac{\pi\omega\epsilon''}{cosh^{-1}(D/2a)} \tag{3.58}$$

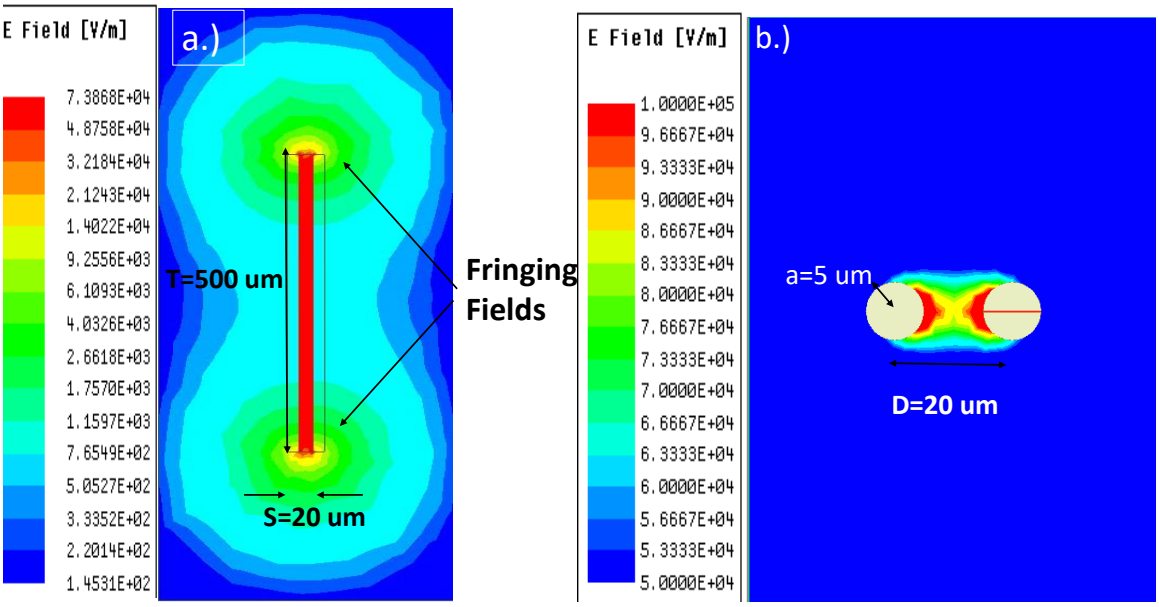

Figure 3.8: a) Magnitude of electric field for a parallel-plate waveguide, b) Magnitude of electric field for a two-wire waveguide

where D is the distance between the center of two wires and a is the radius of each wire. Finally, we can find the complex propagation constant by using Eq. (3.53):

$$\gamma_{TWWG} = \alpha + j\beta = \sqrt{-\omega^2\mu\epsilon' + j\omega\frac{R_s\epsilon'}{a \times cosh^{-1}(D/2a)}} \tag{3.59}$$

The attenuation constant is calculated theoretically with MATLAB for $D = 20\ \mu m$ and $a = 5\ \mu m$ (Figure (3.7)). Since a two-wire waveguide has a circular cross-sectional area and there is no sharp edge like in the case of a parallel-plate waveguide, it does not have fringing electric fields. There is a small discrepancy between the theoretical and simulation results due to the limitations with mesh accuracy.

The amplitude of the electric field for a parallel-plate waveguide is illustrated in

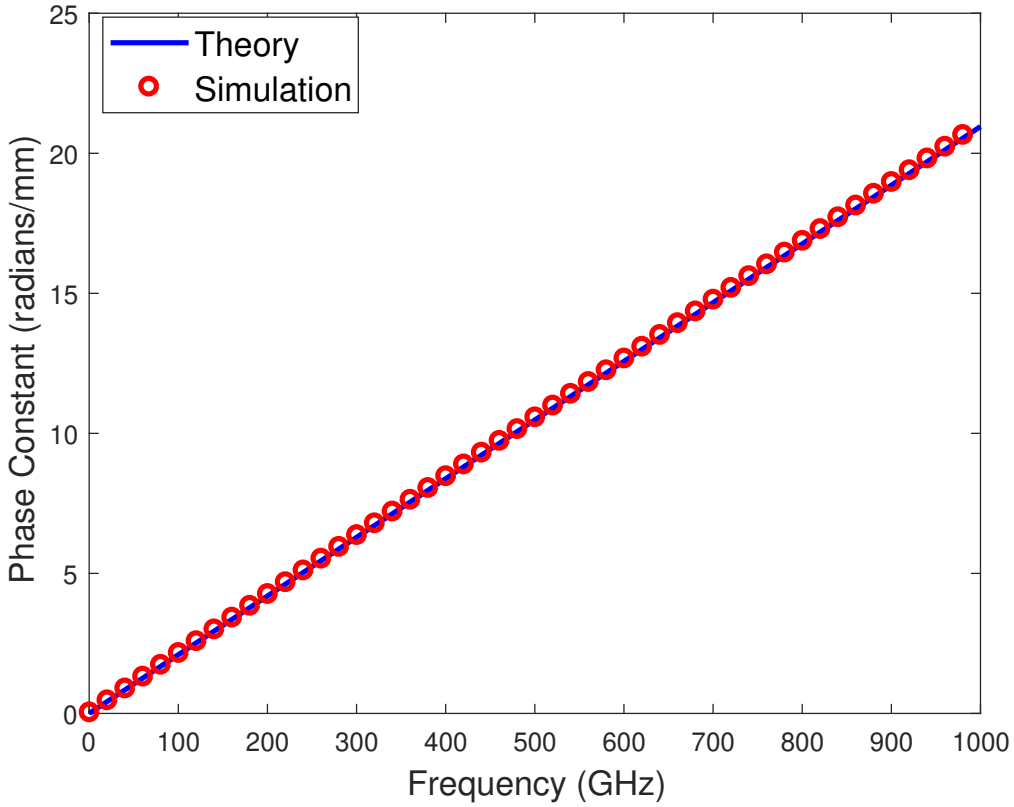

Figure 3.9: Phase constant (β) for a two-wire waveguide with $D = 20\ \mu m$ and $a = 5\ \mu m$

Figure (3.8a) and for a two-wire waveguide in Figure (3.8b). The effect of the fringing field is apparent for the parallel-plate waveguide. Besides, the two-wire waveguide has more field confinement between the metals than the parallel-plate waveguide.

If we assume that there is a vacuum dielectric media for the two-wire waveguide, we can plot its phase constant (β), which is entirely linear. This linearity indicates that there is no dispersion for the guided mode in a two-wire waveguide. Figure (3.9) shows the phase constant for a two-wire waveguide with $D = 20\ \mu m$ and $a = 5\ \mu m$. The theoretical result arises from the imaginary part of Eq. (3.59) and is quite similar

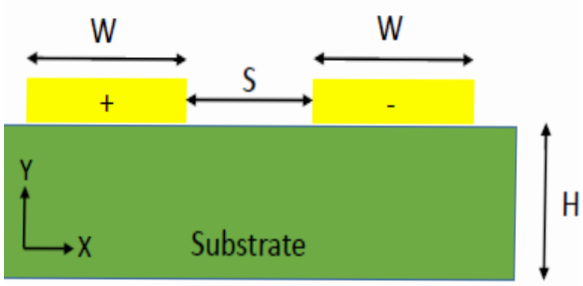

Figure 3.10: Cross-sectional view of a coplanar stripline

to the simulation results.

3.4.3 Coplanar Stripline Waveguides

A coplanar stripline is a planar-type of waveguide that is appropriate for microwave integrated circuits and can be fabricated using photolithographic techniques. A cross-section of a coplanar stripline is illustrated in Figure (3.10). There are two thin conducting strips with a width of W and a separation distance S between them and are mounted on top of a substrate of height H.

Coplanar striplines can support a quasi-TEM wave because it has two conductors and a dielectric (substrate). TEM is the normal mode of operation [35] in coplanar stripline waveguides. A coplanar stripline is usually preferred since it only needs a single-sided metalization on a dielectric substrate. Alternatives such as the microstrip transmission line require a substrate with a two-sized metalization and do not have extensive usefulness in the terahertz region due to the thickness of the substrate [44].

Progress in semiconductor material fabrication has enabled coplanar striplines

to achieve frequency bandwidth response extending beyond 400 GHz [46]. These bandwidths surpass the range of accuracy of the quasi-static approximations which are usually made in modelling the propagation of the electrical signals on transmission line interconnects [11]. The demand for waveguide interconnect modelling and the utilization of the propagation measurements to material characterization requires a well-defined theory of the transmission line attenuation and dispersion properties. Besides, one of the many advantages that this provides is allowing computations to be carried out analytically.

Coplanar striplines originally have three dominant loss mechanisms: dielectric losses, radiation losses, and conductor losses from the finite metalization. The role of each loss needs to be analyzed because at high frequencies attenuation becomes more significant. It has been proved experimentally that the radiative losses are the dominant losses for frequencies over 200 GHz for coplanar waveguides with dimensions of the order of a few tens of microns [15]. Therefore, it is desirable to neutralize the radiation losses' effect in high frequencies.

The attenuation and dispersion properties are shown using empirical models to allow for suitable coplanar stripline designs. We will analyze the effect of dielectric's thickness and metal structure on the dispersion and attenuation. Hence, we will be able to design an appropriate waveguide with almost no dispersion and minimum loss.

Dispersion Characteristics

The dispersive properties of coplanar transmission lines have been modelled empirically [17]. The phase constant is given by:

$$\beta(f) = \frac{2\pi f}{c}\sqrt{\epsilon_{eff}(f)} \tag{3.60}$$

where $\epsilon_{eff}(f)$ is the effective permittivity of the dielectric substrate and is analytically represented as:

$$\sqrt{\epsilon_{eff}(f)} = \sqrt{\epsilon_q} + \frac{\sqrt{\epsilon_r} - \sqrt{\epsilon_q}}{1 + a\left(\frac{f}{f_{te}}\right)^{-b}} \tag{3.61}$$

where ϵ_q (quasi-static effective permittivity)and f_{te} (cut-off frequency for the lowest order TE mode) are respectively given by:

$$\epsilon_q = \frac{\epsilon_r + 1}{2} \tag{3.62}$$

$$f_{te} = \frac{c}{4H\sqrt{\epsilon_r - 1}} \tag{3.63}$$

where c is the speed of light in vacuum, and ϵ_r is the relative permittivity of the substrate material. It has been observed that b (~ 1.8) is independent of the dimensions, while a is computed from the below equation [17]:

$$\log(a) \approx u\ log(S/W) + v \tag{3.64}$$

where

$$u \approx 0.54 - 0.64q + 0.15q^2$$
$$v \approx 0.43 - 0.86q + 0.54q^2 \tag{3.65}$$
$$q = \log(S/H)$$

S, W, and H are the geometric parameters that are shown in Figure (3.10). Figure (3.11) shows the effective permittivity of a coplanar stripline with Silicon Nitride substrate ($\epsilon_r = 7$) as per theory and results of simulation. The effective permittivity increases as frequency increases and it reaches the substrate permittivity at high frequencies. The theoretical results are more accurate than the simulation results since there are mesh resolution limitations in the simulation software. Also, Eq. (3.61) to calculate the effective permittivity only works precisely up until 1 THz [11].

3.4.4 Attenuation Characteristics

Dielectric Loss

The dielectric loss depends on the dielectric loss tangent and frequency. For Silicon Nitride with $f < 1.5\ THz$, the dielectric loss tangent is approximately, $tan\delta = 0.009$. For these amounts, the dielectric loss is less than 0.5 (dB/mm) [13], which is minor in comparison to the other losses.

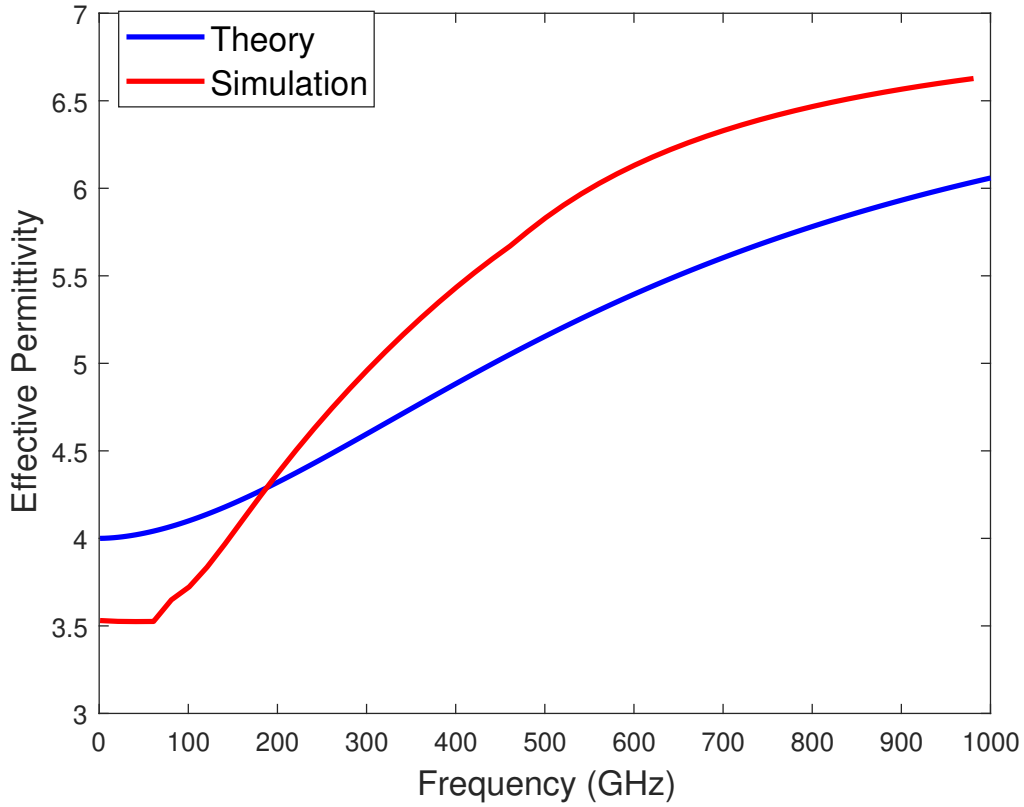

Figure 3.11: Effective Permittivity of a CPS with Silicon Nitride substrate ($\epsilon_r = 7$)

Surface Waves and Radiation Loss

As mentioned before, the radiative losses are the dominant losses for frequencies beyond 200 GHz [15] as well as when the dielectric is thick. It has been shown that the attenuation should follow a cubic frequency dependence under quasi-static approximations [11]. Therefore, the attenuation constant is given by:

$$\alpha_{cps} = \pi^5 \frac{(3-\sqrt{8})}{2} \sqrt{\frac{\epsilon_{eff}(f)}{\epsilon_r}} \left(1 - \frac{\epsilon_{eff}(f)}{\epsilon_r}\right)^2 \frac{(S+2W)^2 \epsilon_r^{3/2}}{c^3 K'(k) K(k)} f^3 \tag{3.66}$$

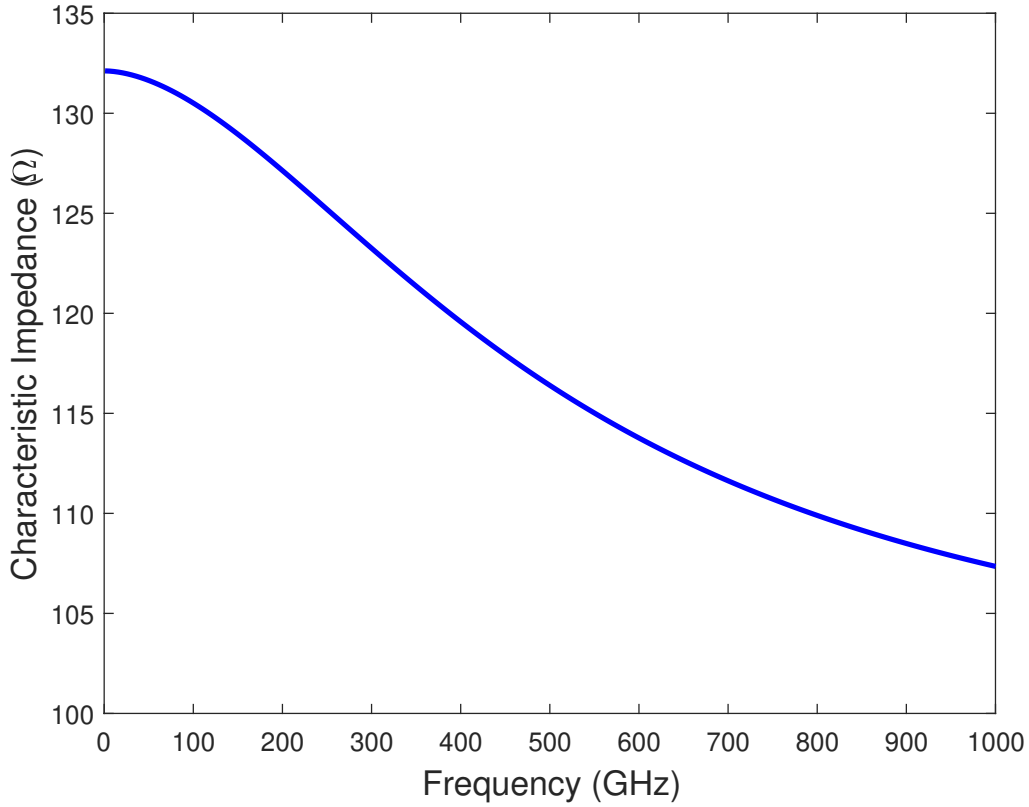

Figure 3.12: Characteristic impedance of a CPS with Silicon Nitride as a substrate

where $k = S/(S+2W)$, $K(k)$ is the complete elliptic integral of the first kind, and $K'(k) = K(\sqrt{1-k^2})$. These equations are expected to be correct for structures which approximately have features dimensions that follow the relation $0.1 < S/W < 10$ and $H > 3W$, and for wavelengths $\lambda > S + 2W$.

ϵ_{eff} reaches ϵ_r at very high frequencies (around 1 THz). ϵ_{eff} is useful as well to compute the characteristic impedance variation with frequency [11]:

$$Z_{cps} = \frac{120\pi}{\sqrt{\epsilon_{eff}(f)}} \frac{K(k)}{K'(k)} \tag{3.67}$$

Figure (3.12) illustrates the characteristic impedance of a coplanar stripline with a Silicon Nitride substrate of 50 μm thickness. The gap between the lines is 10 μm. The characteristic impedance varies between 132 Ω and 107 Ω. The reason for the variation is due to effective permittivity changing when the frequency increases.

The dielectric losses can be neglected for the substrate materials discussed. Also, the conductor losses depend on the square root of the frequency [13], although they are almost negligible compare to the radiation losses. It is virtually possible to eliminate radiation losses by decreasing the dielectric thickness drastically. Although this method is efficient to reduce the losses, it is difficult to practically achieve using photolithography and metal sputtering on such a thin substrate. This approach is also beneficial to avoid dispersion effects since the effective permittivity is close to 1. The electric fields are mostly created in the air instead of inside the dielectric. Hence, the effective permittivity will become so close to the permittivity of air ($\epsilon_r = 1$) [45]. As a result, this type of waveguide will have low dispersion and minimal radiation losses.

Conductor Loss

After appropriate assumptions discussed in the preceding types of losses, conductor loss remains the dominant one. Conductor loss depends on the surface current density and material conductivity [45]. The S/W ratio needs to be analyzed for identifying the minimum conductor loss. Figure (4.1) illustrates attenuation constants for coplanar striplines with different separation distances and widths of metallic lines. Simulation

results imply that the optimum separation distance and width are $S = 70\ \mu m$ and $W = 45\ \mu m$, which results in a ratio of $\frac{S}{W}$=1.55. More discussion about practical methods, such as gradual tapering, for reducing the conductor loss in a coplanar stripline will be detailed in the next chapter.

Chapter 4

Design Optimization of a Coplanar Stripline

4.1 Tapering Method to Reduce The Conductor Loss

In a terahertz coplanar stripline, the distance between the lines should be roughly 10 μm at the excitation zone in the transmitter and receiver areas to minimize radiation and generate terahertz pulses efficiently. Figure (4.1) shows that the attenuation constant is approximately 0.7 (Np/mm) for $S = W = 10\ \mu m$, while it is almost 0.42 (Np/mm) for $S = 70\ \mu m$, $W = 45\ \mu m$ for hundreds of GHz. S and W are the coplanar stripline separation and width shown in Figure (3.10). Therefore, the beginning dimensions of the terahertz coplanar stripline ($S = W = 10\ \mu m$) are not

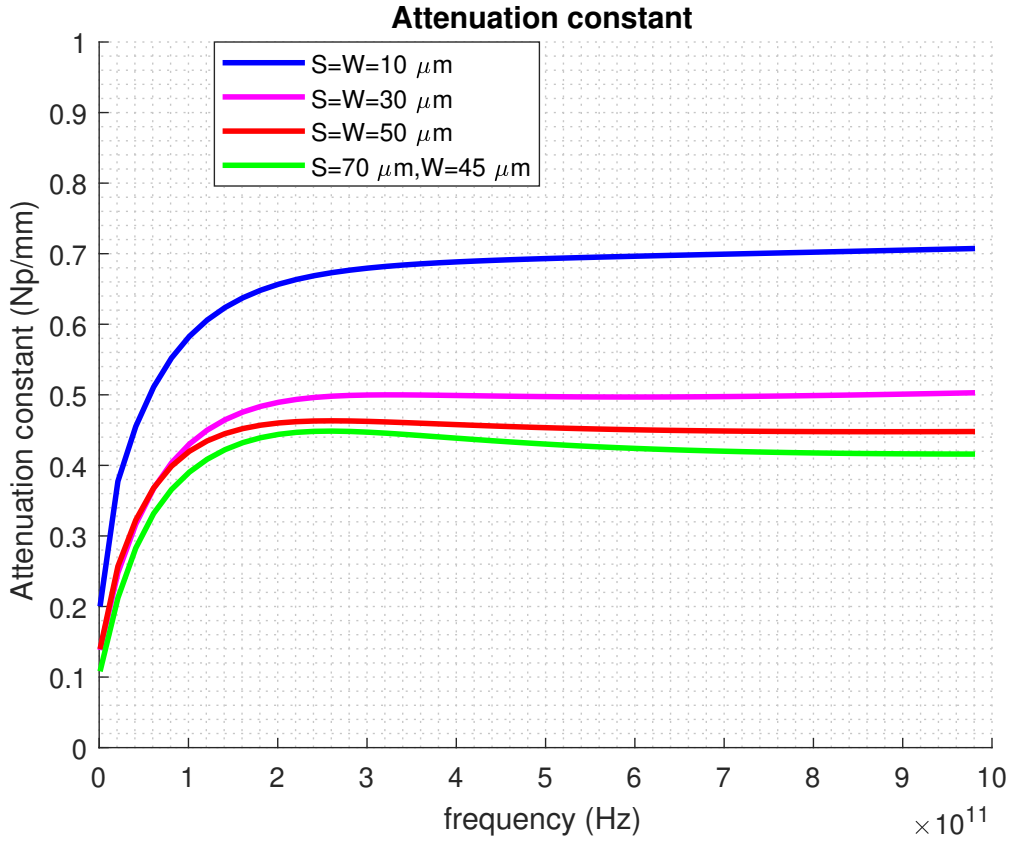

Figure 4.1: Attenuation constants for coplanar striplines with different separation distances and width of metallic lines

optimum to minimize the conductor loss. A smoothly tapered transmission line is an appropriate method to connect the initial dimensions to the optimum dimensions ($S = 70\ \mu m,\ W = 45\ \mu m$) of the coplanar stripline. In other words, a continuously tapered transmission line is a transformer that can match the impedance of the two separate segments of the coplanar stripline, over a broad bandwidth, that have different widths and separations.

Since the tapered transmission line can be utilized at extremely high frequencies or for very short pulses, it has been used broadly in monolithic microwave inte-

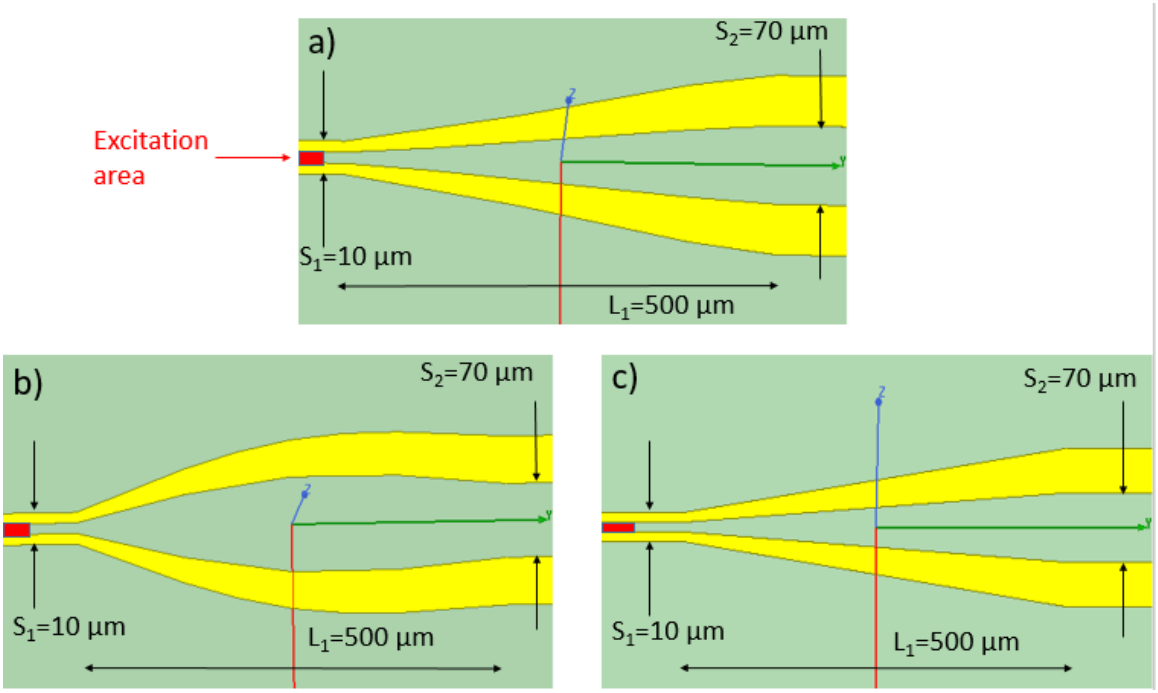

Figure 4.2: Tapered section of a coplanar stripline with a.) Gradual tapering b.) Symmetric tapering c.) Linear tapering

grated circuits (MMICs) and high clock rate digital integrated circuits for impedance transformation [54]. This structure can support broad bandwidth and TEM modes properly. The fields are symmetrical in this structure as well [29]. Moreover, it needs a straightforward fabrication process.

The tapered transmission line acts as an impedance transformer. This impedance transformer matches lower input impedance at the beginning of the stripline to relatively higher impedance of optimum dimensions of the stripline [29]. Hence, it causes some reflection losses in the areas that the impedance changes drastically. There are some discontinuities in the taper edges, where some of the signal power reflects. A desirable tapered transmission line is optimum in the sense that it has minimum

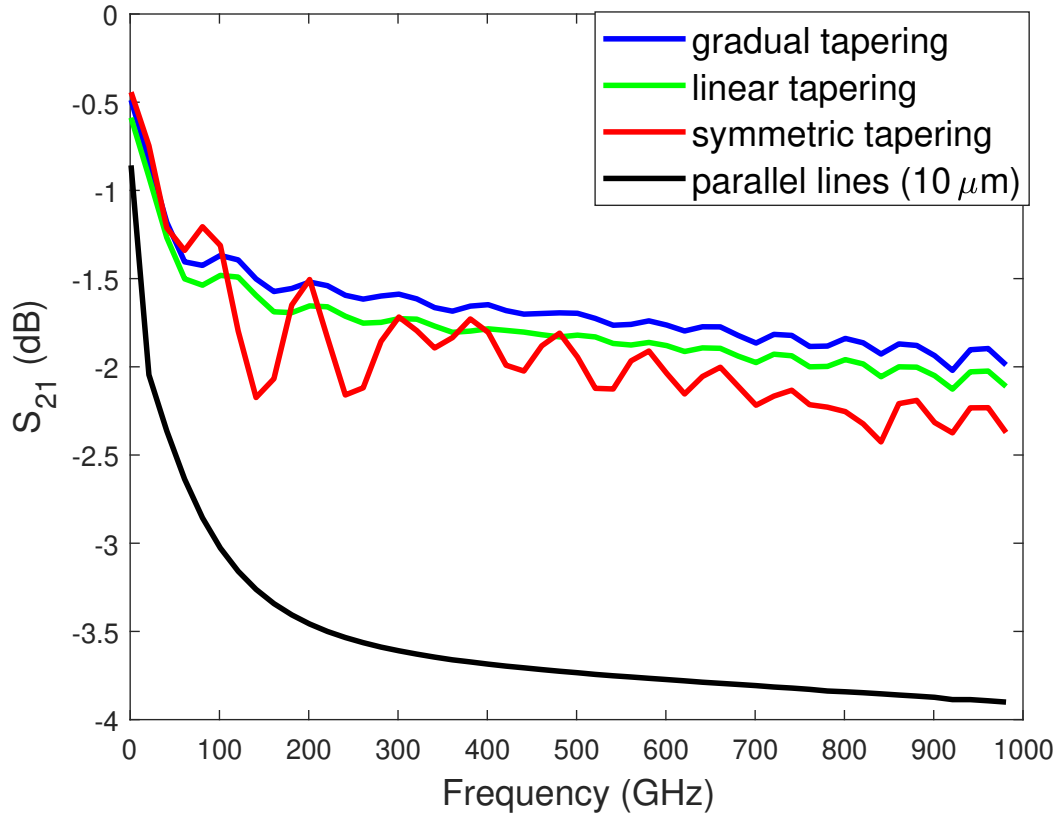

Figure 4.3: S_{21} parameters for a coplanar stripline with different tapering sections

reflection coefficient magnitude for a certain length of taper [26].

Figure (4.2) shows coplanar striplines, where their initial dimensions are $S = W = 10\ \mu m$, then there are tapering sections with 500 μm length, and finally there are parallel lines with $S = 70\ \mu m$, $W = 45\ \mu m$. There are a few types of tapers for coplanar striplines with different configurations. The first one is gradual tapering line (Figure (4.2a)), which smoothly increases the distance between the metal plates. The second one is the symmetric tapering line (Figure (4.2b)), which the slope of increasing the distance between the metal plates is not constant. The third one is

linear tapering line (Figure (4.2c)), and as its name implies, the distance between the metal plates increases linearly.

Figure (4.3) shows S_{21} parameters for coplanar striplines with different types of tapering. The coplanar stripline with gradual tapering has the highest S_{21} (lowest loss) and reflection loss as well. It is shown in this figure that the symmetric tapering has the most reflection loss among all of the mentioned tapers. There are some resonances in the S_{21} parameters coming from reflections between both sides of tapering lines. Also, S_{21} parameter for parallel lines with $S = 10\ \mu m$ and $W = 10\ \mu m$ is plotted in this figure to show the difference between this parallel stripline and tapering striplines. As a conclusion, the S_{21} parameter for a coplanar stripline with gradual tapering has approximately 2 dB less loss than a coplanar stripline with initial dimensions ($S = W = 10\ \mu m$) although there are some resonances in the S_{21} parameter in the tapered striplines.

4.2 RF Components in a Coplanar Stripline

The purpose of this section is to provide details on the various RF components in a coplanar stripline, which can be used in TSOC applications, and discuss optimization of parameters.

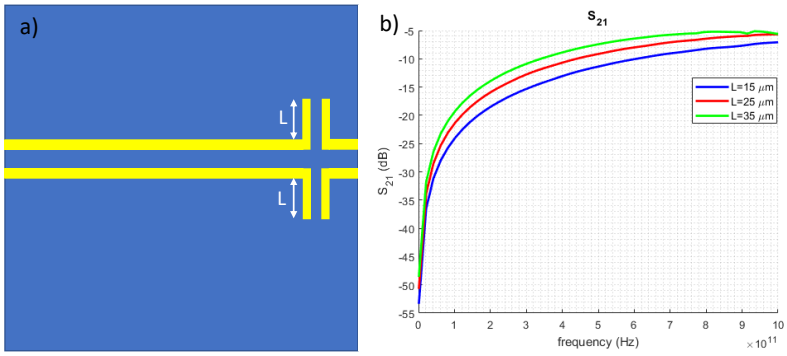

Figure 4.4: S_{21} parameters for coplanar striplines with single stubs

4.2.1 Single Stubs as a DC Block

It is possible to use a single open-circuited length of the transmission line (Figure (4.4a)) as a capacitor, which is connected in series with the main transmission line. According to Figure (4.4b), as the length of the open-circuited transmission line increases, it can block lower frequencies. Indeed, when the length of the stub becomes larger, its capacitance increases. Therefore, the stub's impedance will have lower magnitude. The other considerable point for single stub capacitors is that although it is straightforward to fabricate them, they have more loss than interdigitated electrodes detailed in the next section.

Figure (4.4b) shows the transmission coefficient (S_{21}) for coplanar striplines with

different stub lengths. As it is evident, when we increase the stub length, the transmission coefficient increases (less negative). As a result, we can conclude that the length of the stub has inverse relation with the transmission coefficient. Indeed, as the stub length increases, the electromagnetic coupling in the gap gets better, and waves are transmitted more efficiently.

4.2.2 Interdigitated Electodes as a DC Block

Interdigitated capacitors have been researched widely since the early 1970s. These structures have applications in lumped elements for MMICs. As mentioned in previous sections, the DC voltage which is connected to the transmitter photoconductor should not transfer to the receiver. For this approach, we will use a capacitor in the waveguide to block DC voltages. Since a coplanar stripline is used in this work, interdigitated electrodes are the best options to create a capacitor. Interdigitated capacitors are useful components because of their simplicity of fabrication, relatively high Q, and lower loss than other capacitor designs.

An efficient design of the interdigitated capacitors needs closed-form expressions to determine their capacitance. The capacitance depends on the geometry and the properties of the substrate, such as its permittivity. One of the first designs for the interdigitated capacitors was carried out in 1970 by Alley [1]. According to that model, it is possible to calculate the capacitance values for equal length and gap width. This model has been used until now because experimental results are in

excellent agreement with the suggested procedure of capacitance calculation.

Alley's model was revised in 1979 and a loss expression was proposed into Alley's Theory [19]. Subsequently in 1983, the effect of the thickness of metalization on the capacitance magnitude was investigated [9]. Although these papers are more accurate to compute the capacitance value, they do not have direct formulae, and numerical techniques are required. To make computation easier, it is worth to consider each two adjacent electrodes, as parallel-plate waveguides. Therefore, the capacitance between the two electrodes can be calculated by:

$$C = \epsilon_0 \epsilon_r \frac{A}{d} \tag{4.1}$$

where A is the electrode's surface area and d is the gap between the two adjacent electrodes, ϵ_0 is the permittivity of free space and ϵ_r is the material's relative permittivity between the electrodes. According to this expression, there are 3 factors which can change the capacitance value: (i) by varying the surface area (A), (ii) by changing the gap between two adjacent electrodes (d) and (iii) by altering the material's permittivity between the electrodes (ϵ_r).

To make the capacitance expression simpler, edge effects may be ignored and then capacitance is given by:

$$C = n\epsilon_0 \epsilon_r \frac{ld}{t} \tag{4.2}$$

where n is the number of interdigitated electrodes, l is the length, d is the thickness

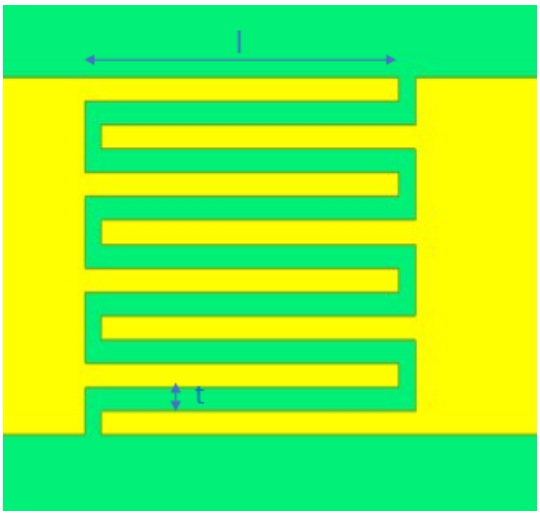

Figure 4.5: Interdigitated electrodes

and t is the gap between the electrodes (Figure (4.5)).

For a case that electrodes have tens of micrometers length and less than 10 $\mu\ m$ gap between them, the capacitance is in order of femtofarad. It means that electrodes can block frequencies until a few hundreds of GHz. Therefore, they are efficient to implement in a Terahertz waveguide to block DC voltages and low-frequency signals.

The characteristic impedance of a usual terahertz coplanar stripline waveguide is between 200-300 Ω. On the other hand, the impedance of these interdigitated electrodes is given by:

$$Z = \frac{1}{j2\pi fC} \tag{4.3}$$

where f is the frequency that varies from 0 to a few terahertz in this case. If we consider the interdigitated electrodes with the specific dimensions mentioned in the last paragraph, the capacitor impedance will be neglectable after 300 GHz compared

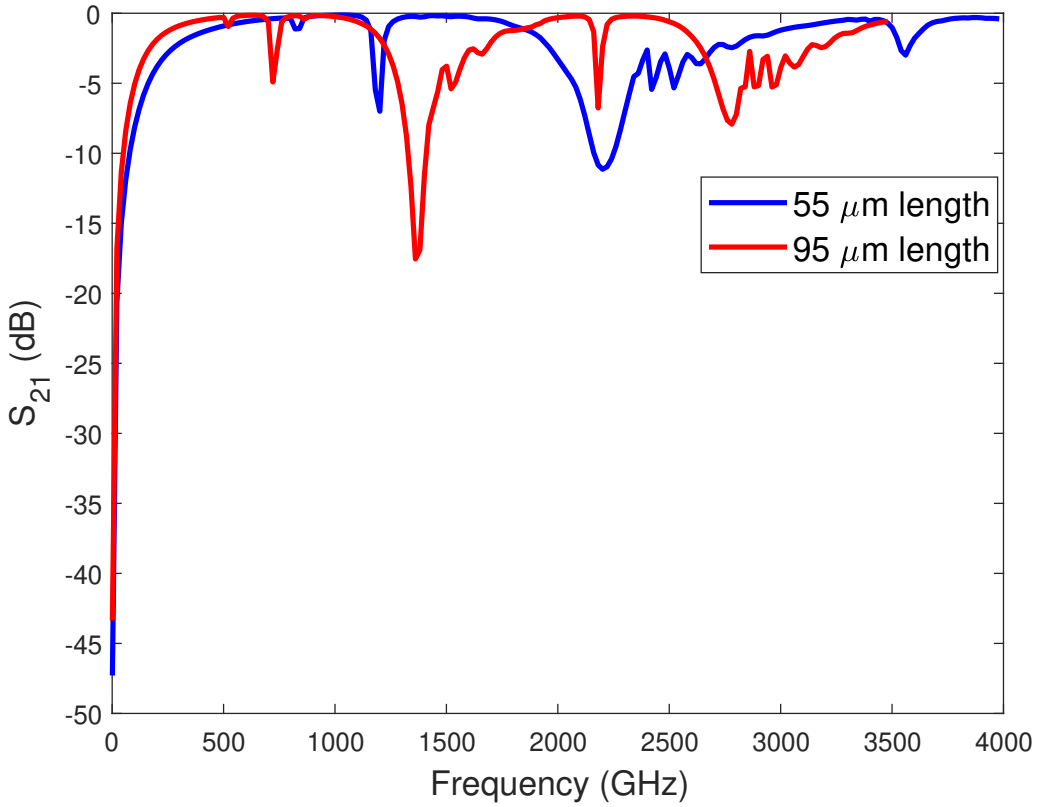

Figure 4.6: S_{21} (dB) for interdigitated electrodes with 95 μm and 55 μm length and 5 μm separation

to the coplanar stripline characteristic impedance. Hence, these interdigitated electrodes are able to act as a high pass filter and block DC voltages and low-frequency signals as well.

In Figure (4.6), S_{21} diagram for interdigitated electrodes is shown. S_{21} demonstrates high pass filter characteristics of the interdigitated capacitor. Moreover, there are some peaks in the spectrum due to the existence of resonant frequencies. The

formula to calculate resonant frequency is given by:

$$f_r = \frac{1}{2\pi\sqrt{LC}} \tag{4.4}$$

where C is the total capacitance of electrodes and L is the inductance for the electrode unit. Interdigitated electrodes are considered to behave as an inductor and a capacitor. To confirm the origin of the peaks, the results from Figure (4.6) show that when the length of electrodes increases, the capacitance enhances as well. Hence, the resonant frequencies decrease.

There are some design limitations for the interdigitated electrodes. A noticeable limitation is the breakdown voltage. Beyond a threshold electric field, called the dielectric strength E_{ds}, the dielectric in a capacitor becomes conductive. The voltage at which it happens is called the breakdown voltage of the capacitor and depends on the dielectric strength (E_{ds}) and the distance between the conductors. The formula to calculate the breakdown voltage is given by [47]:

$$V_{bd} = E_{ds}d \tag{4.5}$$

where d is the gap between conductors.

The breakdown voltage restricts the maximum energy that can be stored in a capacitor. All capacitors built with a specific dielectric have a very close maximum

energy density because of the scaling of capacitance and breakdown voltage with dielectric thickness. For capacitors which have air as their dielectric, the breakdown field strength is in the order of $2-5\ \frac{MV}{m}$; for Silicon Nitride (membrane of choice in this work) the breakdown is $300-900\ \frac{MV}{m}$ [34]. As the voltage increases, the dielectric should be thicker, making high-voltage capacitors larger to avoid breakdown.

In our work, we have a very thin dielectric, which is Silicon Nitride (Si_3N_4), and structures like interdigitated electrodes are mounted on top of it. In a cross-section view, there is only air between electrodes. Therefore, most of the electric field is created through the air between electrodes, and we can consider air as the predominant dielectric in this case. The smallest gap between the electrodes should be a few microns not to have any breakdown voltage in the waveguide.

The other factor that limits the design of interdigitated electrodes is the fabrication technique to mount gold electrodes on the top of the membrane. Photolithography is the standard method for fabricating these waveguides but it limits the minimum feature size attainable. To reach lower resolutions, Focused Ion Beam (FIB) micromachining technique can be adopted. This method uses extremely focused Gallium-ion beams to scan and form the substrate by milling the metal.

4.2.3 RF Chokes and Bias Tees

A regular inductor is made by wrapping wires around a solid rod or a cylindrical ring which is the inductor core. When current flows inside the wires, a magnetic flux is

created that opposes the change in current. The magnetic flux induces a voltage in the coil. The intensity of the magnetic flux depends on the type of core [39].

RF chokes are considered as applications of inductors. They are fixed inductors to block high-frequency alternating current (AC) signals and let the low-frequency and DC signals pass. To attain this goal, the choke (or the inductor) should have a large impedance over the range of frequencies it is designed to block.

When we combine a capacitor and an RF choke with a specific configuration, bias tee is created. Bias tees are the elements that are utilized to supply DC currents or voltages to bias RF circuits. A bias tee has three ports. An equivalent circuit of it can be seen in Figure (4.7). Signals that consist of RF + DC are incident at port one. The capacitor suppresses all DC signals from passing through to port two and only allows the AC/RF Signals to pass through. Although some bias tees can be manufactured with a simple inductor and capacitor, wideband bias tees are noticeably more complex since practical components have parasitic elements.

If we imagine having a line with a characteristic impedance Z_0, the impedance of the capacitor (X_C) is selected to be much less than Z_0, and the impedance of the inductor (X_L) is chosen to be much larger than Z_0:

$$X_C = \frac{1}{\omega C} = \frac{1}{2\pi f C} \ll Z_0 \tag{4.6}$$

$$X_L = \omega L = 2\pi f L \gg Z_0 \tag{4.7}$$

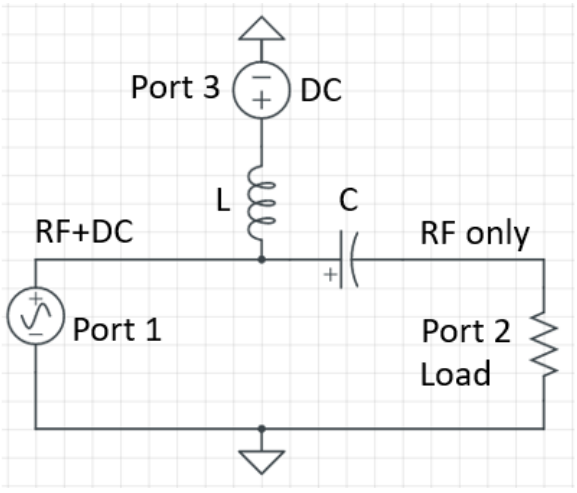

Figure 4.7: Bias tee equivalent circuit

where ω is the angular frequency (in radians per second), and f is the frequency (in hertz). In other words, a bias tee can be considered as a diplexer with an ideal capacitor that lets AC passes through and a perfect inductor that blocks AC but allows DC. DC voltage signal can pass through the inductor to drive the circuit while the AC voltage signal is not able to pass it since the RF signal has to reach to the receiver in the waveguide and it should not have significant leakage into the DC bias section of the waveguide.

In our work, we make an inductor with the meander structure (Figure (4.8)) that is similar to interdigitated electrodes. Meander structures can store electromagnetic energy and act as high Q-factor inductors. The formula to compute its inductance is given by [3]:

$$L = 0.0026a^{0.0603}h^{0.4429}N^{0.954}d^{0.606}W^{-0.173} \tag{4.8}$$

where L is the inductance (μH), N is the number of turns, a is the length of the

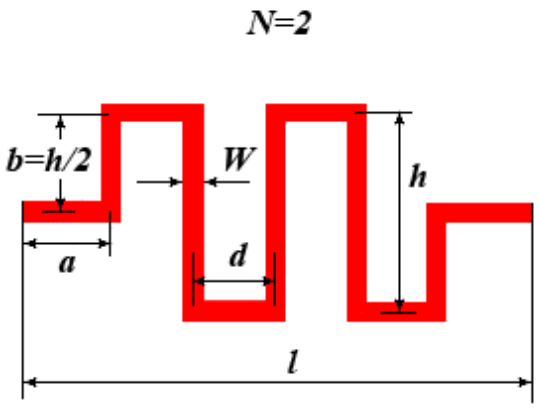

Figure 4.8: Meander structure as an inductor [3]

lead (mm), h is the height of meander (mm), d is the width of meander (mm), W is the width of the printed strip (mm). In our design, h is 100 μm (0.1 mm), N is 20, W is 5 μm (0.005 mm), d is 5 μm (0.005 mm), and a is 5 μm (0.005 mm). Therefore, the inductance is approximately is 1 nH.

There is some optimization required to effectively design the capacitor and inductor for bias tees. First of all, the length of the interdigitated electrodes should be optimized to have lower return loss. According to Eq. (4.4), the structure does not allow signals to pass the waveguide at the resonant frequency. Therefore, it is better to tune the capacitance and inductance to have a resonant frequency of lower than 200 GHz to not affect the main spectrum of RF signals.

It is possible to adjust the resonant frequency and shift it to lower frequencies, although there are some restrictions due to the theoretical and fabrication aspects. When we want to have lower resonant frequencies, we have to either increase the

length or decrease the gap between the electrodes. However, it is too risky to reduce the gap size less than 3 μm because the breakdown voltage might happen in the interdigitated electrodes area and destroy the waveguide. Besides, the cost of fabrication for small gaps is expensive.

Figure (4.6) shows S_{21} (dB) for two coplanar stripline waveguides with bias tees. They have different interdigitated electrode lengths. For both curves the intensities start from -50 dB, and after passing 100 GHz, reach -3 dB approximately. Therefore, it is clear that these structures can block lower frequencies and act as a high pass filter, which is our goal. Although they have the same intensity through most of the spectrum, they have different peaks. The resonant frequencies come from electrodes features (not from meander structure). The first peaks for each curve are relevant to the resonant frequencies in an LC circuit (Eq. (4.4)). It means that interdigitated electrodes act as an inductor in high frequencies, in addition to be capacitors initially. When we increase the length of the electrodes, capacitance increases as stated by Eq. (4.2). Therefore, the resonant frequency decreases, which agrees with the theory (Eq. (4.4)).

We can compute the resonant frequency for each length of electrodes using Eq. (4.2) and Eq. (4.8) to calculate the capacitance and inductance, respectively. After that, we will apply Eq. (4.4) to find the resonant frequencies. The capacitances and inductances are 0.08 pF and 1.17 nH for shorter interdigitated electrodes while 0.048 pF and 0.91 nH for the longer electrodes. Therefore, the resonant frequencies are

507 GHz and 752 Ghz, respectively. On the other hand, the resonant frequencies are 521 GHz and 825 Ghz in simulation results (Figure (4.6)). Hence, theoretical values are fairly close to simulation results, and the small difference between them is due to this fact that the formula to calculate the capacitance ignores the edge effects of electrodes. Edge effects are included in the simulation.

The other peaks come from some reflections through the waveguide. Waveguide behaviours are more difficult to predict in high frequencies than lower frequencies. The area that the interdigitated electrodes are located acts as a cavity [20]. Signals with certain frequencies oscillate inside this area; hence, some resonant peaks in S_{21} spectrum are created. The formula to calculate the resonant frequency for this cavity is given by:

$$f_f = \frac{c}{2nl} \tag{4.9}$$

where c is the speed of light in a vacuum ($3 \times 10^8 \ \frac{m}{s}$), n is the refractive index of the substrate, and l is the length of the cavity. In our case, since we use a membrane as a substrate, the refractive index is close to 1 (1.1 as attained by simulation), and l is the length of interdigitated electrodes. The resonant frequencies are 2.3 THz for shorter electrodes and 1.36 THz for longer electrodes which are close to peaks in simulation results (Figure (4.6)). The other dimension of interdigitated electrodes also plays a role as a Fabry–Pérot interferometer, where l is 45 μm (width of each stripline) and the resonant frequency is 3.33 THz. This resonant frequency is true

due to the simulation results as well.

4.2.4 Bandstop Filters in the Terahertz Region

A bandstop filter or bandrejection filter transfers most frequencies without any attenuation but attenuates those in a special range to low levels. It is the opposite of a bandpass filter. The bandstop filter is built by the combination of high pass and low pass filters with a parallel configuration.

As the name implies, it will stop a particular band of frequencies. Bandpass and bandstop filters have two cut-off frequencies, unlike high pass and low pass filters. It will pass a particular range of frequencies whose cut-off frequencies are determined by the elements utilized in the circuit design. Frequencies between these two cut-offs are attenuated. In other words, it has two passbands and one stopband.

In coplanar waveguides, some structures have bandstop filter properties. We will introduce and analyze one of these structures here: split-ring resonators.

Split-Ring Resonators

Split-ring resonators (SRRs) have become an interesting research topic since they were introduced [33] for producing artificial magnetism phenomena. These resonant particles have enabled the possibility of creating artificial structures (also called metamaterials) which can have atypical electromagnetic characteristics [49]. The chance of producing artificial structures that can create negative refraction opens the way to

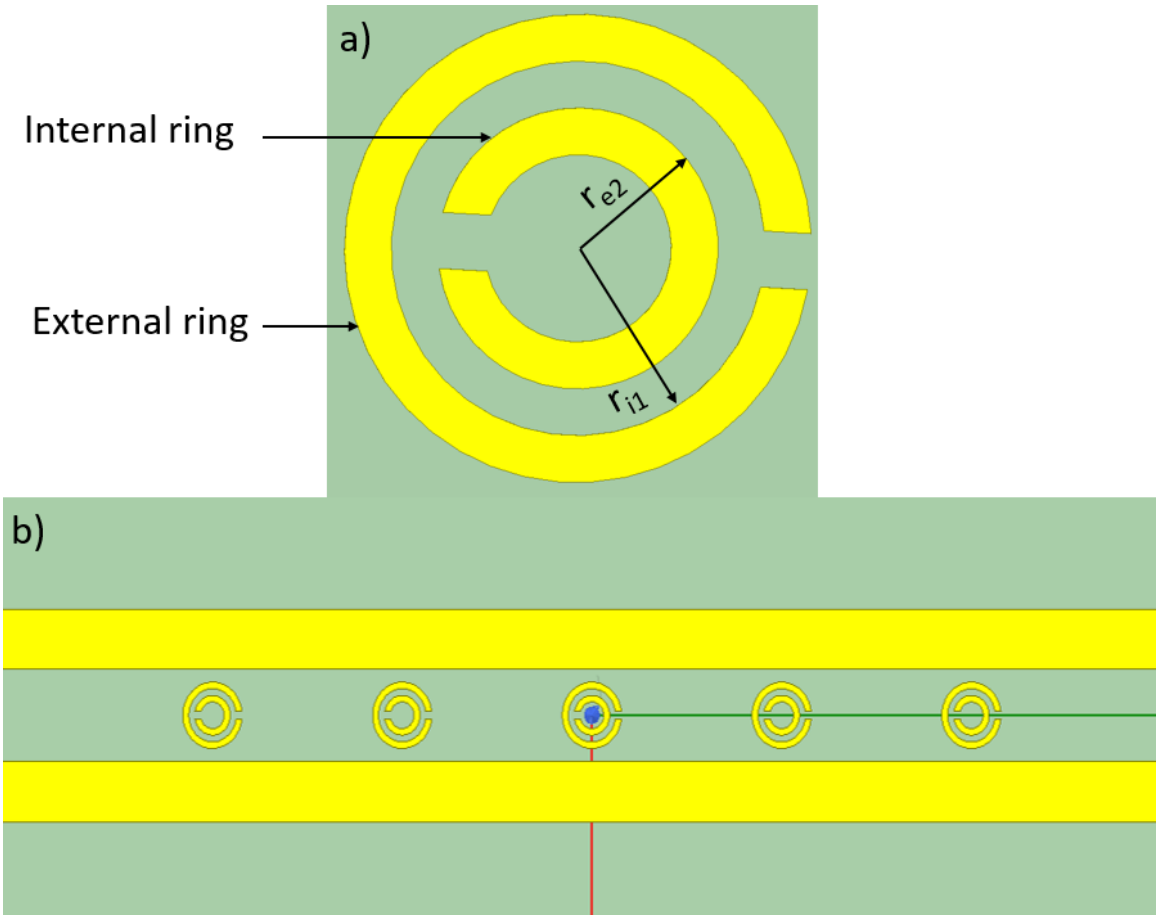

Figure 4.9: a) Split-ring resonator, b) Split-ring resonators utilized in a coplanar stripline waveguide

a novel range of devices in refracted, radiated or guided applications. These unique features are artificially produced by integrating a negative effective permeability and a negative effective permittivity simultaneously in a specific frequency range. The resonant operation of the split-ring resonators properly combined with other components, depending on the technology applied, generates narrow frequency bands where this double-negative condition can be achieved. The split-ring resonators have been widely considered in terms of resonant properties, which can be utilized in a band-stop

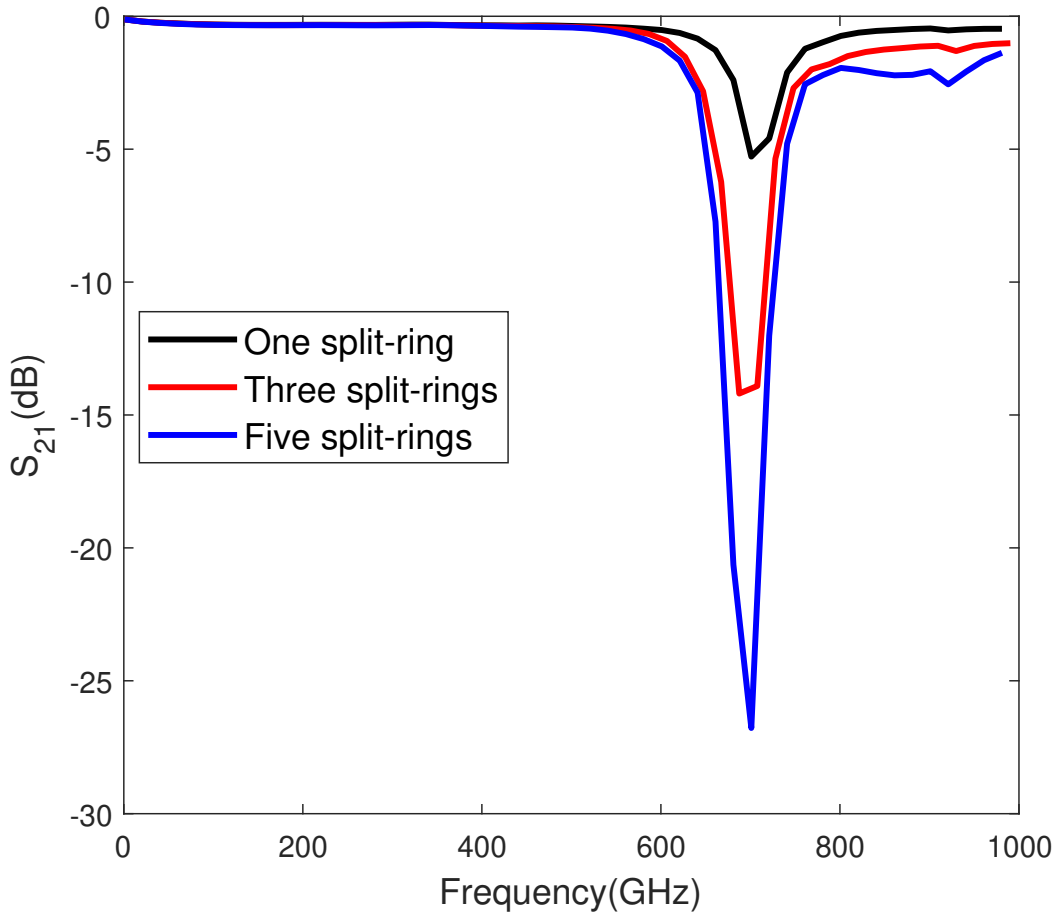

Figure 4.10: S_{21} parameter for a coplanar stripline with different number of split-rings as a bandstop filter

filter [38].

Calculating Resonant Frequency

A simple analytical computation for the resonant frequency of the split ring resonator configuration was provided by [36]:

$$f_r = \sqrt{\frac{3d}{\pi^2 r}} \frac{v_p}{r} \frac{1}{2\pi} \tag{4.10}$$

and

$$d = r_{i1} - r_{e2} \tag{4.11}$$

$$r = \frac{r_{i1} + r_{e2}}{2} \tag{4.12}$$

where r_{i1} is the internal radius of the outer ring, r_{e2} is the external radius of the inner ring (Figure (4.9)), and v_p is the speed of light in the coplanar waveguide's medium ($v_p = \frac{c_0}{\sqrt{\epsilon_{eff}}}$). In our work, the radius of the rings should be less than 35 μm in order to embed between the coplanar plates. As an example, if we select $r_{i1} = 25$ μm and $r_{e2} = 20$ μm, the resonant frequency will be 701 GHz, which is located in the terahertz region.

Figure (4.10) shows S_{21} parameter for a coplanar stripline with different number of split-rings. As the number of split-rings increases, the amplitude of S_{21} increases at the resonant frequency. Also, the $-3dB$ bandwidth of the filter becomes narrower and the filter will be sharper while increasing the number of split-rings. In other words, when the number of rings increases, the Q factor increases as well. As a result, the stopband is narrower and the filter is more selective.

Figure (4.11) shows the electric field for a coplanar stripline with split-ring resonators. The electric field is illustrated for two different frequency regions. Figure

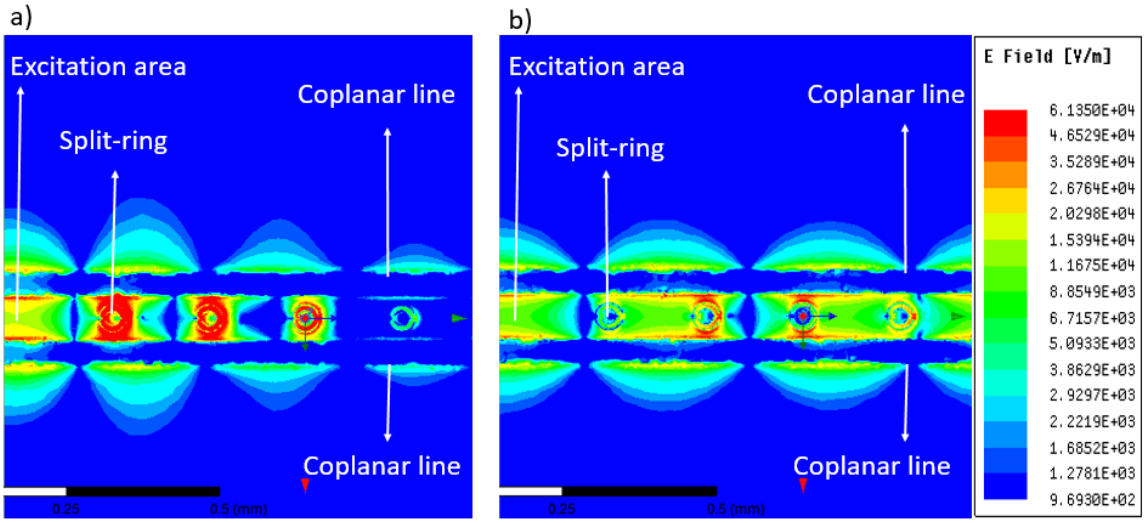

Figure 4.11: The electric field of a coplanar stripline with split-ring resonators a.) In the band-stop frequency region b.) In the band-pass frequency region

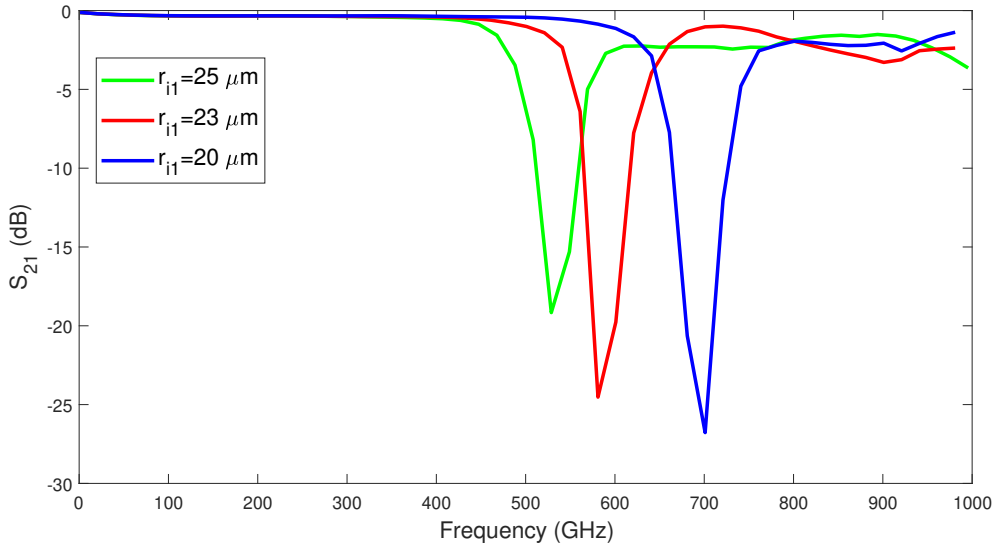

Figure 4.12: S_{21} parameter for a coplanar stripline with different radii of the split-rings

(4.11a) shows suppression of the electric field in the band-stop region and Figure (4.11b) depicts passing the electric field along the waveguide with low losses in the

band-pass region.

Figure (4.12) illustrates S_{21} parameter for a coplanar stripline with different split-ring radii. The internal radii (r_{i1}) are 25 μm, 23 μm, and 20 μm, respectively. The theoretical resonant frequencies for each of the radii are 546 GHz, 614 GHz, 699 GHz, respectively, which is close to simulation results. Hence, when the split-ring radii increase, the resonant frequency decreases.

4.3 Finding Waveguide Behaviour from Multiplying the ABCD Matrix

As mentioned in previous chapters, we can find the total ABCD matrix of a complex two-port structure by multiplying the individual simpler two-port networks together in a cascade connection. This method is also useful for a coplanar stripline, which includes RF components such as capacitors, inductors, and tapered sections. The main advantage of this technique is that sometimes it is too difficult to determine a complicated waveguide's behaviour by a single simulation due to restricted computational resources.

To calculate the total ABCD matrix of our system, first we need to find each component's ABCD matrix. ABCD parameters can be determined by both simulation and theoretical computation for some simple components. For complex components, we only use simulation results. It is also noteworthy to compare simulation and theo-

retical results to have a better understanding of each waveguide's element. Therefore, we will analyze parallel lines, and tapered sections separately.

It is valuable to show the relation between S parameters and ABCD parameters since the ANSYS HFSS only provides the S parameters directly, and we need to obtain ABCD parameters from them. The relations are provided by [12]:

$$A = \frac{(1 + S_{11})(1 - S_{22}) + S_{12}S_{21}}{2S_{21}} \tag{4.13}$$

$$B = Z_0 \frac{(1 + S_{11})(1 + S_{22}) - S_{12}S_{21}}{2S_{21}} \tag{4.14}$$

$$C = \frac{1}{Z_0} \frac{(1 - S_{11})(1 - S_{22}) + S_{12}S_{21}}{2S_{21}} \tag{4.15}$$

$$D = \frac{(1 - S_{11})(1 + S_{22}) + S_{12}S_{21}}{2S_{21}} \tag{4.16}$$

where Z_0 is the characteristic impedance of the connected transmission line.

4.3.1 ABCD matrix for parallel lines

The ABCD parameters for the parallel plate sections of a coplanar stripline in lossless conditions are given by [35]:

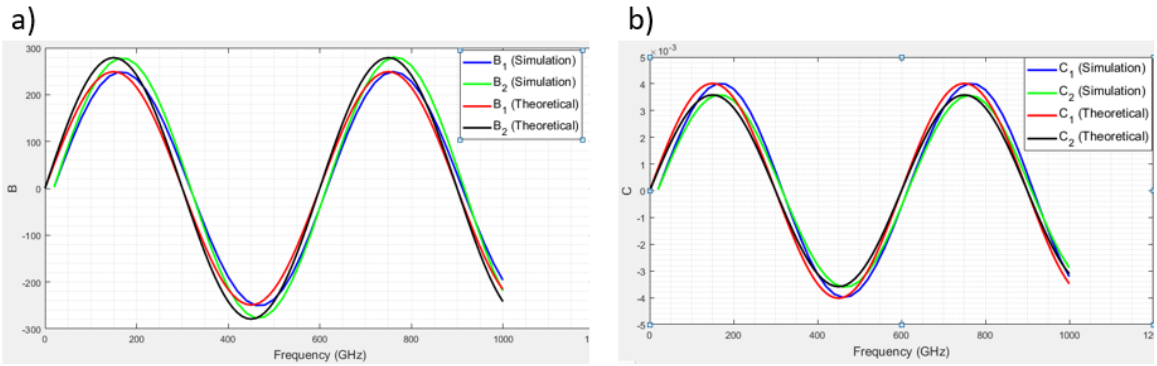

Figure 4.13: Theoretical and simulation results for parallel lines with $s_1 = 10\ \mu m$, $w_1 = 10\ \mu m$, $s_2 = 70\ \mu m$, $w_2 = 45\ \mu m$: a) Imaginary parts of B parameters, b) Imaginary parts of C parameters

$$A = cos(\beta l), \tag{4.17}$$

$$B = jZ_0 sin(\beta l), \tag{4.18}$$

$$C = jY_0 sin(\beta l), \tag{4.19}$$

$$D = cos(\beta l), \tag{4.20}$$

where Z_0 is the characteristic impedance of the line, Y_0 is the characteristic admittance of the line, and l is the length of the line.

Figure (4.13) shows ABCD parameters for parallel lines with different width and

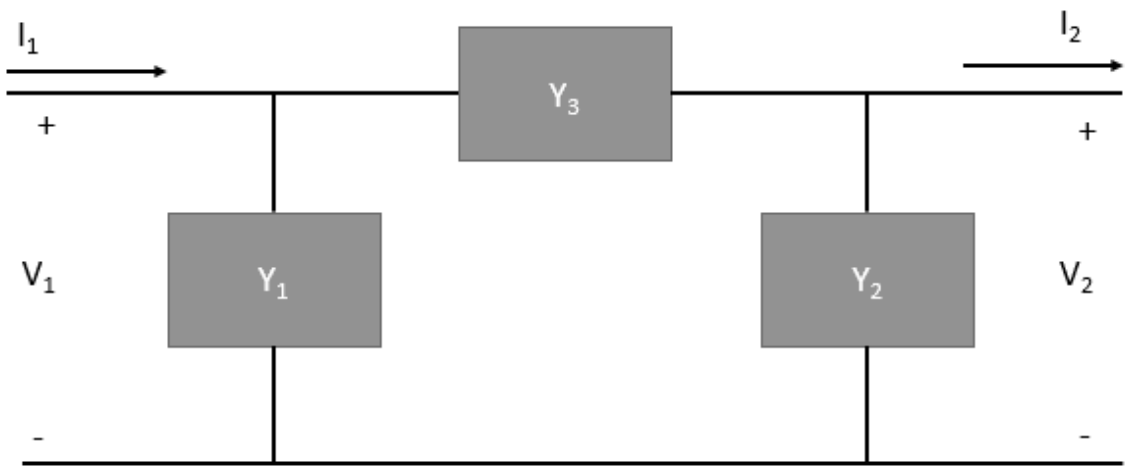

Figure 4.14: The equivalent circuit for interdigitated electrodes unit

separation. The characteristic impedance can be calculated for each parallel structure using Eq. (3.67). Simultaneously, Figure (4.13) illustrates ABCD parameters derived from S parameters , Eq. (4.13)-Eq. (4.16), and by ANSYS HFSS. The theoretical and simulated figures are almost identical.

4.3.2 ABCD Matrix for Interdigitated Electrodes

Interdigitated electrodes unit can be modelled by an equivalent circuit combined with parallel and series reactive admittances (Figure (4.14)). The ABCD parameters for this equivalent circuit are given by [35]:

$$A = 1 + \frac{Y_2}{Y_3} \tag{4.21}$$

$$B = \frac{1}{Y_3} \tag{4.22}$$

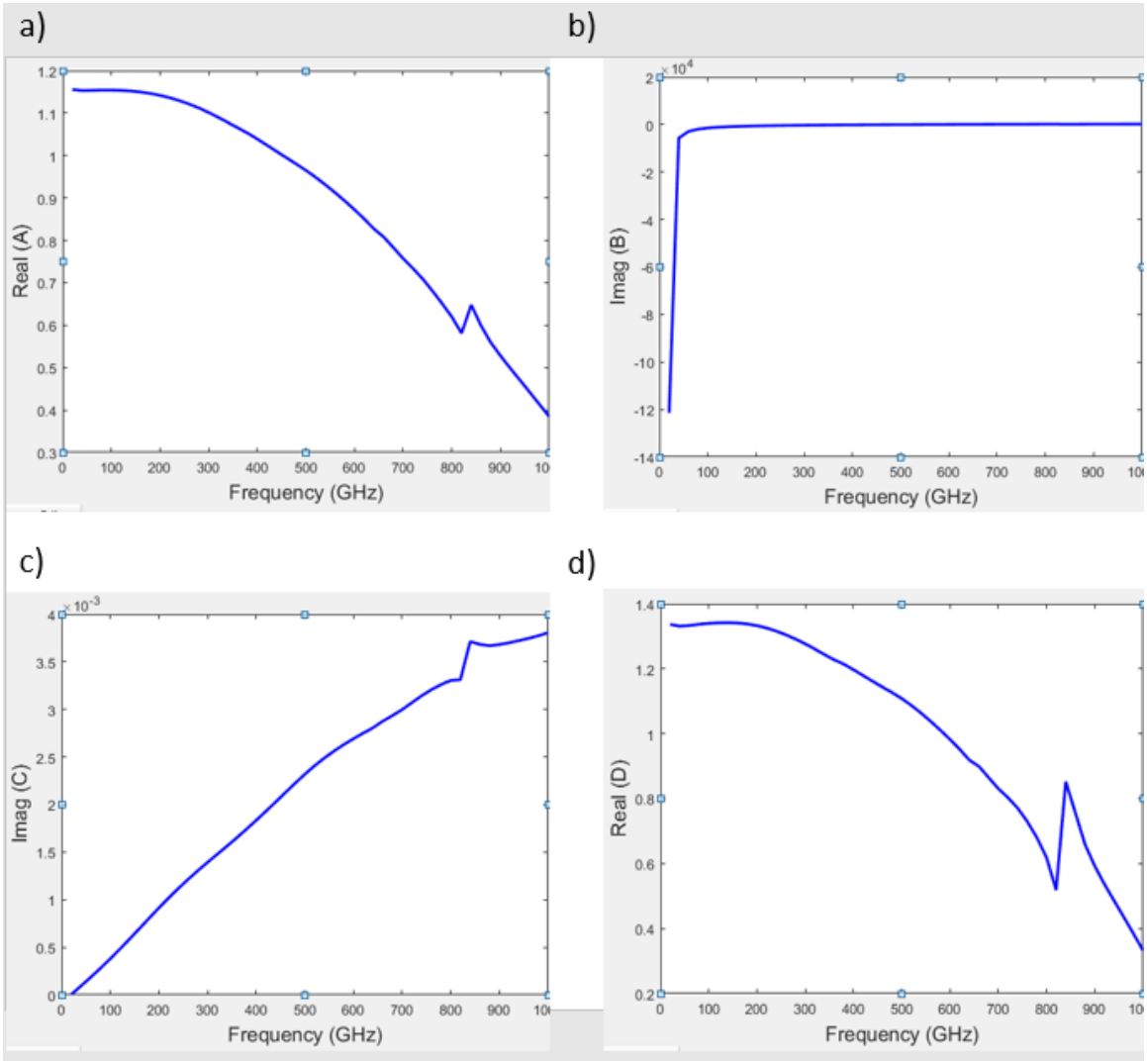

Figure 4.15: ABCD parameters for the interdigitated electrodes unit a) Real part of A parameter b) Imaginary part of B parameter c) Imaginary part of C parameter d) Real part of D parameter

$$C = Y_1 + Y_2 + \frac{Y_1 Y_2}{Y_3} \tag{4.23}$$

$$D = 1 + \frac{Y_1}{Y_3} \tag{4.24}$$

It is difficult to determine the relevant admittances (Y_1, Y_2, and Y_3) for the equiv-

alent circuit of interdigitated electrodes due to different types of capacitance existing in this structure. Therefore, it is not easy to find ABCD parameters for the interdigitated electrodes in a coplanar stripline by mathematical computations, and simulation results are needed to be used to obtain ABCD parameters. Figure (4.15) illustrates the ABCD parameters for the interdigitated electrodes unit. From this figure, a discontinuity at 825 GHz is observed in each ABCD parameter. This arises from the resonances that occur in the interdigitated electrodes and can be explained using the capacitor-inductor analogy discussed in previous sections. The interdigitated electrodes act as a capacitor and inductor simultaneously and have resonant frequencies that can be expressed by Eq. (4.4). The B parameter depicted in Figure (4.15b) is also proportional to the impedance of the interdigitated electrodes since the B parameter is the ratio of the voltage of port 1 over the current of port 2 when the voltage of port 2 is zero. The B parameter can be expressed as the ratio of voltage over current that is relevant to the impedance of the structure. This manifests as a high pass filter behaviour from the interdigitated electrodes structure.

4.3.3 ABCD Matrix for a Coplanar Stripline with Integrated Components

It is time to connect different parts of a transmission line such as parallel lines, tapering lines, and interdigitated electrodes and build a system for TSOC applications.

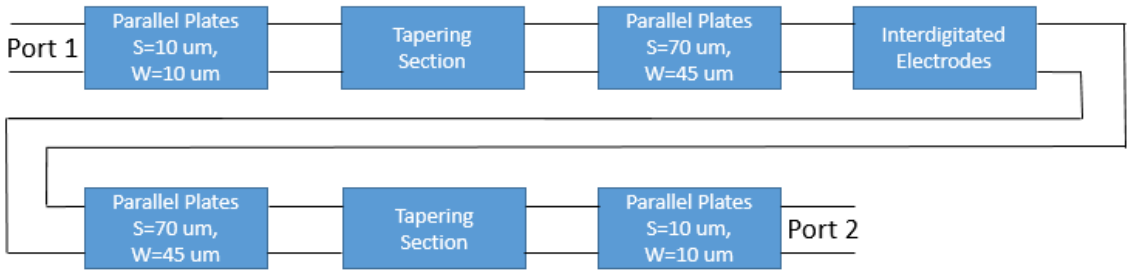

Figure 4.16: The block diagram of the total terahertz system

There are some relatively simple equations to calculate the ABCD matrix for parallel lines, but it is difficult to compute the ABCD matrix for a tapered line and interdigitated electrodes. Therefore, we use only simulation results to calculate the ABCD parameters for the last two parts.

The entire system block diagram, for which we seek to find the ABCD matrix, is shown in Figure (4.16): Firstly, there is a parallel line section with $S_1 = 10\ \mu m$ and $W_1 = 10\ \mu m$. This section has a high loss due to the small separation of parallel lines. Secondly, a gradually tapered section is connected to the first section of the waveguide to increase the separation and width of the lines or decrease the conductor loss. Thirdly, there is a parallel line section with $S_2 = 70\ \mu m$ and $W_2 = 45\ \mu m$, which is connected to the tapered section. The interdigitated electrodes are applied in the middle of this part of the coplanar stripline with 5 μm gap between the adjacent electrodes. Consequently, there will be a tapered section that is connected inversely to the third section, and finally, there will be a parallel line section at the end of the waveguide with the same dimensions as the first section of the waveguide.

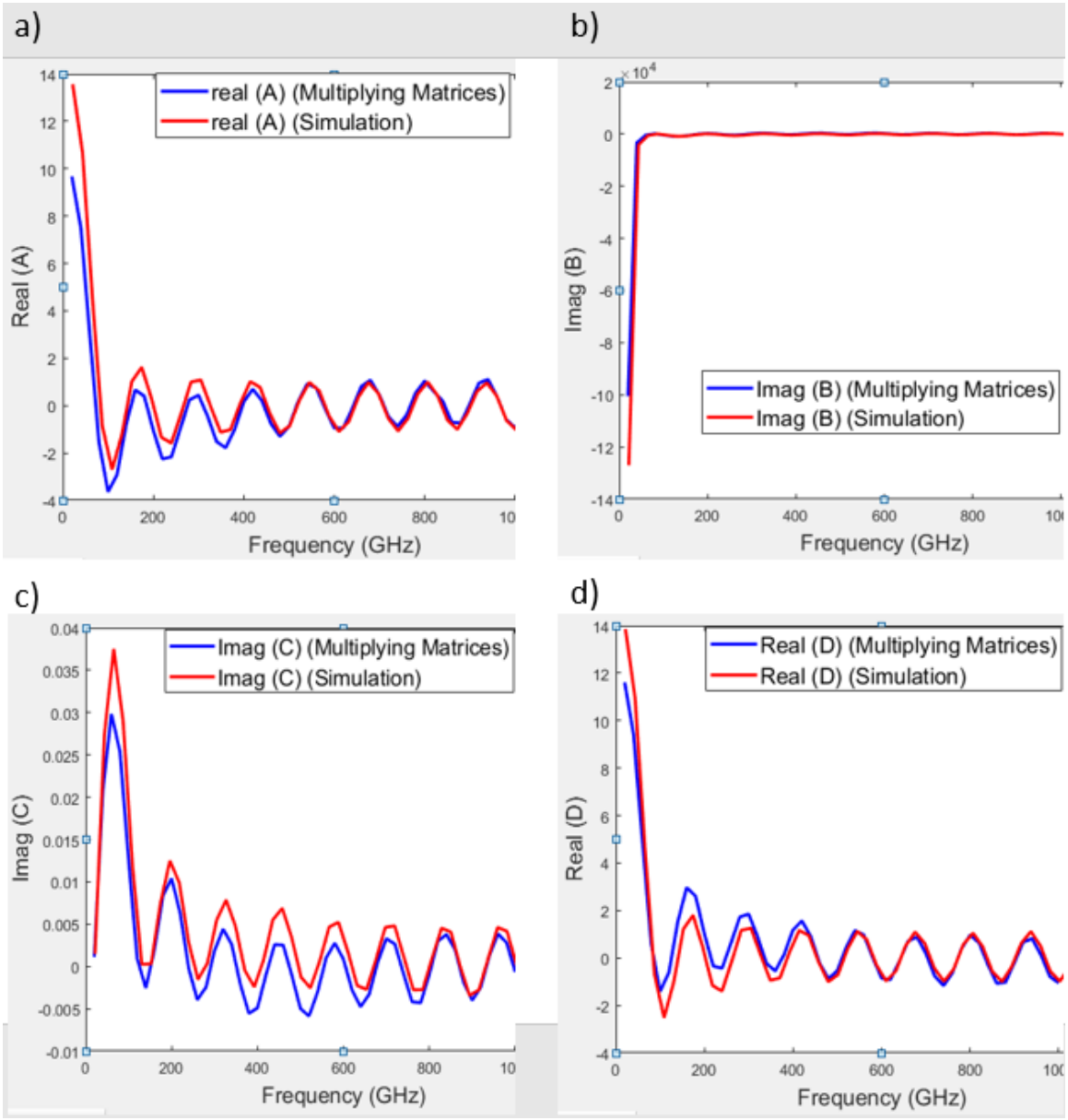

Figure 4.17: The ABCD matrix of a complicated waveguide a) Real part of A parameter b) Imaginary part of B parameter c) Imaginary part of C parameter d) Real part of D parameter

Figure (4.17) illustrates the ABCD matrix for the coplanar stripline, which was described in the last paragraph with two methods. The first method is deriving the ABCD matrix directly from simulation of the total structure. The second method

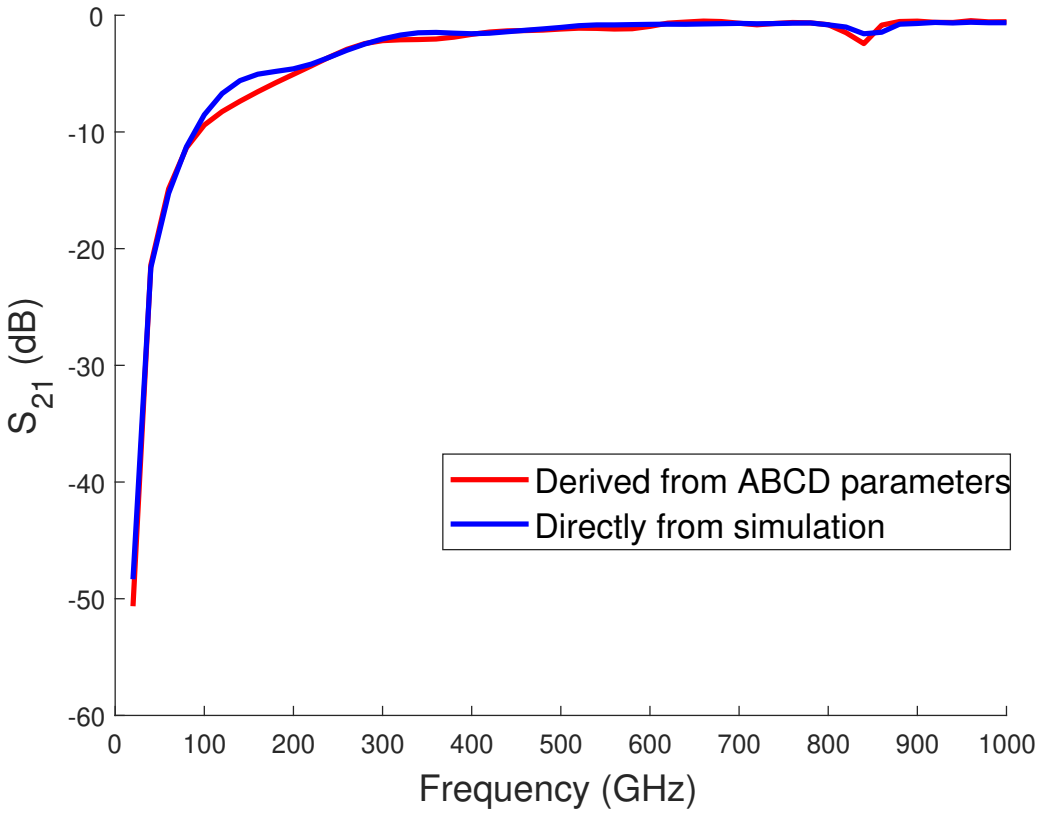

Figure 4.18: S_{21} parameter for a coplanar stripline with two different methods: a)Derived from ABCD parameters b) Directly from simulation

is deriving the ABCD matrix from multiplying the ABCD matrices of the cascade sections, respectively. This has far greater utility since many different circuits can be synthesized by cascading components selected from a library. Results from both methods are very similar. For the calculations carried out for the designs detailed in this work, there exists a negligible difference between the results from two methods due to the limitation on mesh size configuration possible in the software (ANSYS HFSS) due to the finite computing capacity available.

The S parameters can be found when ABCD parameters are known. S_{21} is given

by [35]:

$$S_{21} = \frac{2}{A + B/Z_0 + CZ_0 + D} \tag{4.25}$$

Finally, Figure (4.18) shows the S_{21} parameter derived from resulting ABCD parameters by using Eq. (4.25). Therefore, this method will provide S parameters at the end, and it is useful when for otherwise difficult calculations due to restricted computational resources.

4.4 Final Optimized TSOC

The purpose of this section is to highlight various RF components on a coplanar stripline to build a TSOC. It is worth to mention that all the components have been optimized to reduce loss and dispersion.

Figure (4.19) shows the final design for the TSOC, which is a coplanar stripline on top of a thin dielectric membrane (Si_3N_4). A femtosecond laser is incident between the gold lines at the beginning of the waveguide, where LTG-GaAs is mounted on the membrane. One of the lines is biased by a DC-voltage and therefore, terahertz signals are generated due to the acceleration of electrons and holes in the electric field. Terahertz waves are mostly confined between the gold lines and need to be transferred. At the beginning of the coplanar strips, the separation of the gold lines is $s = 10\ \mu m$, to enable efficient terahertz waves transfer. A high loss results from the small gap between the lines. Therefore, we use gradual tapering to increase the

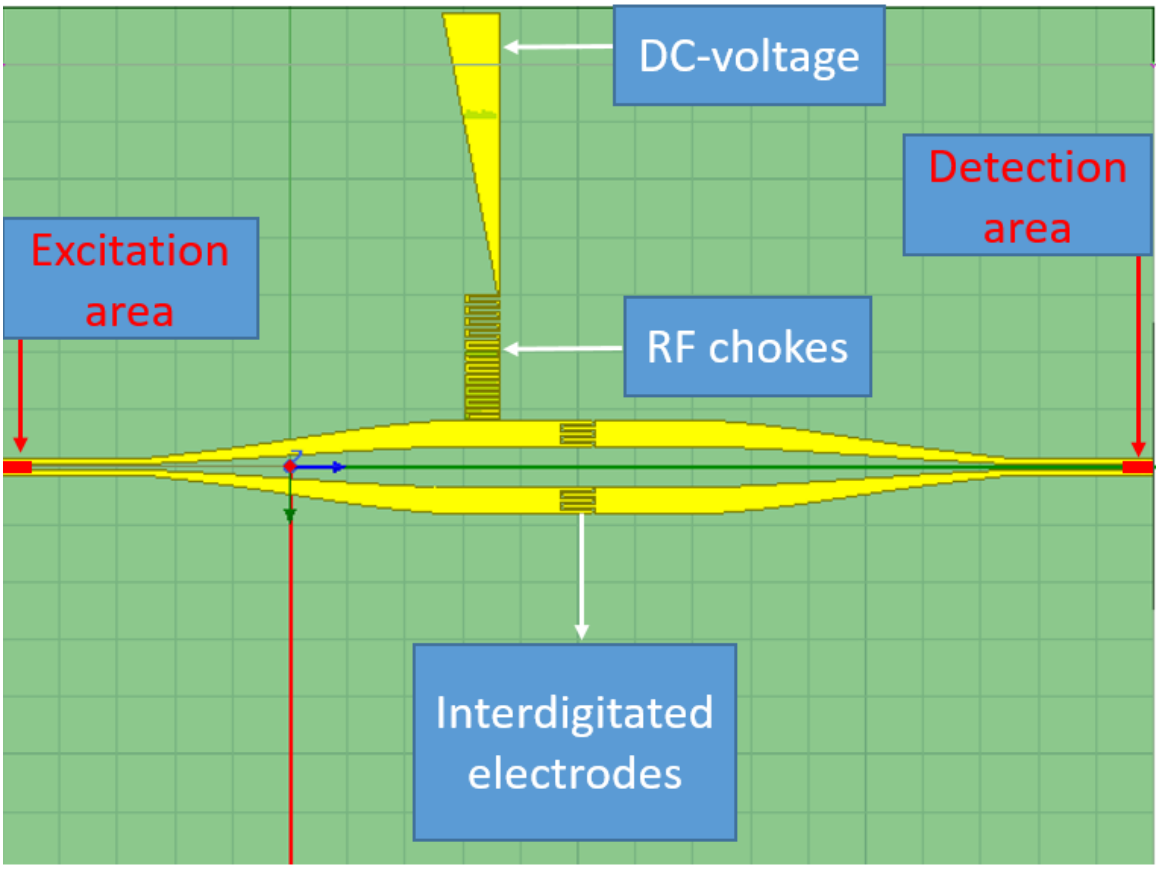

Figure 4.19: The final design of the terahertz waveguide

separation of the gold lines ($s = 70\ \mu m$) and decrease the conductor loss. After that, there will be a bias tee unit which includes interdigitated electrodes and RF chokes. RF chokes act as an inductor that allows DC signals to pass to drive the waveguide, although they do not let RF signals to pass in order to prevent any power leakage. Interdigitated electrodes also act as a capacitor to block DC voltages that should not reach the receiver. Again, there will be another tapering to decrease the separation between the lines to enable terahertz detection at the receiver. In the detection region, a femtosecond laser is incident between the gold lines, where LTG-GaAs is deposited

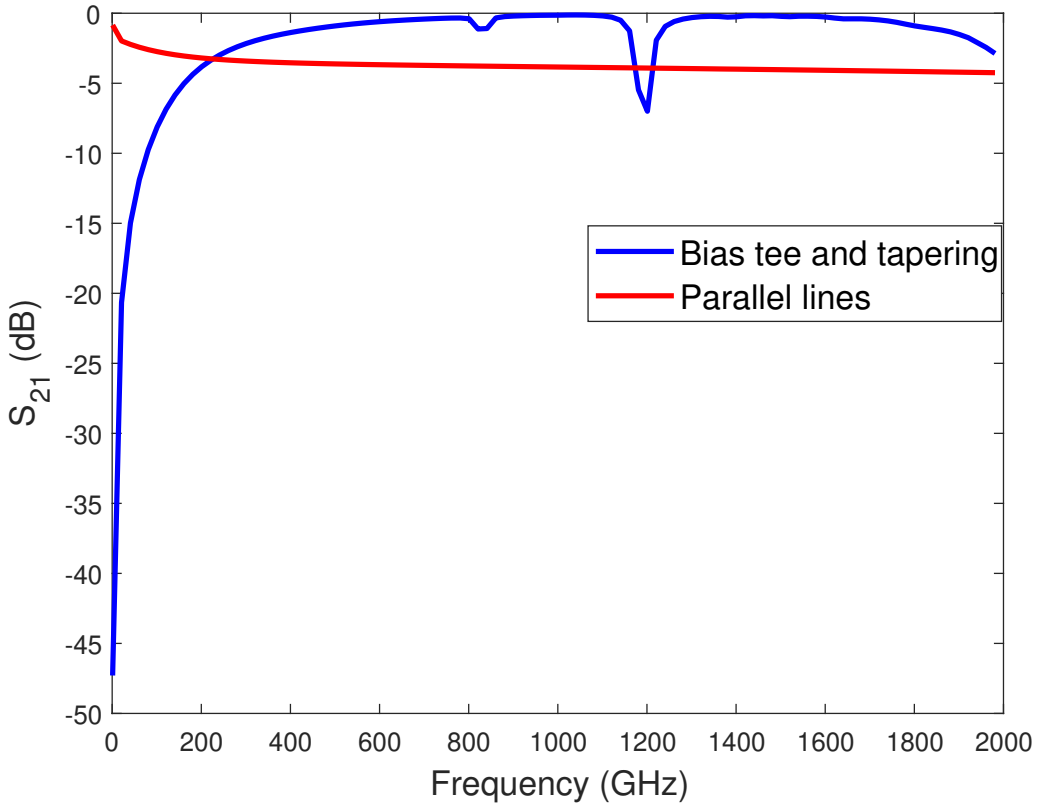

Figure 4.20: S_{21} parameter for the entire terahertz waveguide with tapering and biase tee, and a coplanar stripline with 10 μm separation between the gold lines through whole of the waveguide

on the membrane. As a result, terahertz signals are detected per the process detailed in chapter 2.

Finally, Figure (4.20) illustrates S_{21} parameter for the designed TSOC with the characteristics mentioned in the preceding paragraph. Also, the S_{21} parameter for a coplanar stripline with 10 μm separation throughout the waveguide (previous work [42]) is presented in the figure to compare the loss between the designed TSOC and previous work. The optimized terahertz waveguide design has lower loss than a simple

coplanar stripline with 10 μm separation. However, it has some resonant frequencies due to the effect of capacitors and inductors in the bias tee and tapering sections. Hence, the discussed optimized design is efficient and appropriate for TSOC applications.

Chapter 5

Contributions and Conclusion

5.1 Contributions

A key focus of this research thesis is designing a TSOC by using the advantages of design discussed in previous works and solving the challenges they faced. This work investigates minimizing conductor losses of a coplanar strip transmission line by using gradual tapering. This method increases the gap between the gold plates gradually to achieve the low loss. This thesis also discusses the potential of building TSOCs. Passive components such as a bias tee and a bandstop filter are designed and optimized to work in tandem with other components in the circuit. The bias tee unit includes interdigitated electrodes and a meander type inductor. The interdigitated electrodes are designed to have minimum conductor losses and block DC-voltages appropriately. Split-ring resonators are designed as a bandstop filter and the split-ring dimensions

are shown to vary in relation to the resonant frequency. Moreover, a method is shown to compute the performance of complex terahertz circuits from a library of ABCD matrices of each cascaded component. This technique was widely investigated at microwave frequencies, but not previously considered at terahertz frequencies.

5.2 Conclusion

The work detailed in this thesis focuses on designing terahertz waveguides with low loss and dispersion by optimizing the design so as to overcome inherent losses due to material and geometric limitations. Coplanar striplines are chosen as the optimal waveguide for developing highly efficient TSOCs. This thesis investigates the characteristics of these waveguides using theory and simulations. The contribution of the thesis is regarding the design optimization of various types of passive components used along with a gold coplanar stripline on a Silicon Nitride membrane. A bias tee (a combination of interdigitated electrodes and a meander inductor) is designed to block low frequencies. Split-ring resonators are used as band-stop filters with the optimized design made possible by varying the internal and the external radii of the rings. A final optimized TSOC design is presented that makes use of these passive components and is found to have a total loss less than any of the previous work for terahertz frequencies. This shows great promise for terahertz applications and furthers the horizon for future research in optimizing novel passive and active designs

for TSOCs.

Bibliography

[1] Gary D Alley. Interdigital capacitors and their application to lumped-element microwave integrated circuits. *IEEE Transactions on Microwave Theory and Techniques*, 18(12):1028–1033, 1970.

[2] ER Brown, FW Smith, and KA McIntosh. Coherent millimeter-wave generation by heterodyne conversion in low-temperature-grown gaas photoconductors. *Journal of Applied Physics*, 73(3):1480–1484, 1993.

[3] Coil32, Plugin meandr PCB Inductor on PCB as a meander structure.

[4] J Cunningham, C Wood, AG Davies, I Hunter, EH Linfield, and HE Beere. Terahertz frequency range band-stop filters. *Applied Physics Letters*, 86(21):213503, 2005.

[5] L Dazhang, J Cunningham, MB Byrne, S Khanna, CD Wood, AD Burnett, SM Ershad, EH Linfield, and AG Davies. On-chip terahertz goubau-line waveguides with integrated photoconductive emitters and mode-discriminating detectors. *Applied Physics Letters*, 95(9):092903, 2009.

[6] L Desplanque, JF Lampin, and F Mollot. Generation and detection of terahertz pulses using post-process bonding of low-temperature-grown gaas and algaas. *Applied physics letters*, 84(12):2049–2051, 2004.

[7] Lionel Duvillaret, Frédéric Garet, J-F Roux, and J-L Coutaz. Analytical modeling and optimization of terahertz time-domain spectroscopy experiments, using photoswitches as antennas. *IEEE Journal of Selected Topics in Quantum Electronics*, 7(4):615–623, 2001.

[8] Mario D'Auria, William J Otter, Jonathan Hazell, Brendan TW Gillatt, Callum Long-Collins, Nick M Ridler, and Stepan Lucyszyn. 3-d printed metal-pipe rectangular waveguides. *IEEE Transactions on Components, Packaging and Manufacturing Technology*, 5(9):1339–1349, 2015.

[9] Reza Esfandiari, Douglas W Maki, and Mario Siracusa. Design of interdigitated capacitors and their application to gallium arsenide monolithic filters. *IEEE Transactions on Microwave Theory and Techniques*, 31(1):57–64, 1983.

[10] Bradley Ferguson and Xi-Cheng Zhang. Materials for terahertz science and technology. *Nature materials*, 1(1):26–33, 2002.

[11] Michael Y Frankel, Shantanu Gupta, Janis A Valdmanis, and Gerard A Mourou. Terahertz attenuation and dispersion characteristics of coplanar transmission

lines. *IEEE Transactions on microwave theory and techniques*, 39(6):910–916, 1991.

[12] Dean A Frickey. Conversions between s, z, y, h, abcd, and t parameters which are valid for complex source and load impedances. *IEEE Transactions on microwave theory and techniques*, 42(2):205–211, 1994.

[13] Ramesh Garg, Inder Bahl, and Maurizio Bozzi. *Microstrip lines and slotlines*. Artech house, 2013.

[14] Ian S Gregory, Colin Baker, William R Tribe, Ian V Bradley, Michael J Evans, Edmund H Linfield, A Giles Davies, and Mohamed Missous. Optimization of photomixers and antennas for continuous-wave terahertz emission. *IEEE Journal of Quantum electronics*, 41(5):717–728, 2005.

[15] D Grischkowsky, IN Duling III, JC Chen, and C-C Chi. Electromagnetic shock waves from transmission lines. *Physical review letters*, 59(15):1663, 1987.

[16] Daniel R Grischkowsky. Optoelectronic characterization of transmission lines and waveguides by terahertz time-domain spectroscopy. *IEEE Journal of Selected Topics in Quantum Electronics*, 6(6):1122–1135, 2000.

[17] G Hasnain, A Dienes, and JR Whinnery. Dispersion of picosecond pulses in coplanar transmission lines. *IEEE Transactions on Microwave Theory and Techniques*, 34(6):738–741, 1986.

[18] Louise Ho, Michael Pepper, and Philip Taday. Terahertz spectroscopy: Signatures and fingerprints. *Nature Photonics*, 2(9):541, 2008.

[19] John L Hobdell. Optimization of interdigital capacitors. *ITMTT*, 27:788–791, 1979.

[20] Md Islam, Muhammad Mahmood Ali, Man-Hong Lai, Kok-Sing Lim, Harith Ahmad, et al. Chronology of fabry-perot interferometer fiber-optic sensors and their applications: a review. *Sensors*, 14(4):7451–7488, 2014.

[21] Tae-In Jeon, Jiangquan Zhang, and D Grischkowsky. Thz sommerfeld wave propagation on a single metal wire. *Applied Physics Letters*, 86(16):161904, 2005.

[22] Peter Uhd Jepsen and Bernd M Fischer. Dynamic range in terahertz time-domain transmission and reflection spectroscopy. *Optics letters*, 30(1):29–31, 2005.

[23] Yun-Sik Jin, Geun-Ju Kim, and Seok-Gy Jeon. Terahertz dielectric properties of polymers. *Journal of the Korean Physical Society*, 49(2):513–517, 2006.

[24] Afshin Jooshesh. *Plasmonic-enhanced THz generation and detection using photoconductive antennas*. PhD thesis, 2016.

[25] Keysight. Basics of measuring the dielectric properties of materials, Application Note, 2017.

[26] Ralph W Klopfenstein. A transmission line taper of improved design. *Proceedings of the IRE*, 44(1):31–35, 1956.

[27] Swen Koenig, Daniel Lopez-Diaz, Jochen Antes, Florian Boes, Ralf Henneberger, Arnulf Leuther, Axel Tessmann, René Schmogrow, David Hillerkuss, Robert Palmer, et al. Wireless sub-thz communication system with high data rate. *Nature photonics*, 7(12):977, 2013.

[28] Yun-Shik Lee. *Principles of terahertz science and technology*, volume 170. Springer Science & Business Media, 2009.

[29] Ting-Huei Lin and Ruey-Beei Wu. Cpw to waveguide transition with tapered slotline probe. *IEEE Microwave and Wireless components letters*, 11(7):314–316, 2001.

[30] Andrey Markov and Maksim Skorobogatiy. Plasmonic two wire terahertz fibers with porous dielectric support. In *2013 38th International Conference on Infrared, Millimeter, and Terahertz Waves (IRMMW-THz)*, pages 1–2. IEEE, 2013.

[31] Marx Mbonye, Rajind Mendis, and Daniel M Mittleman. A terahertz two-wire waveguide with low bending loss. *Applied Physics Letters*, 95(23):233506, 2009.

[32] Hamid Pahlevaninezhad. *Design and implementation of efficient terahertz waveguides*. PhD thesis, 2012.

[33] John B Pendry, Anthony J Holden, David J Robbins, and WJ Stewart. Magnetism from conductors and enhanced nonlinear phenomena. *IEEE transactions on microwave theory and techniques*, 47(11):2075–2084, 1999.

[34] A Piccirillo and AL Gobbi. Physical-electrical properties of silicon nitride deposited by pecvd on iii–v semiconductors. *Journal of The Electrochemical Society*, 137(12):3910–3917, 1990.

[35] David M Pozar. *Microwave engineering*. Publishing House of Electronics Industry, 2006.

[36] A Radkovskaya, M Shamonin, CJ Stevens, G Faulkner, DJ Edwards, E Shamonina, and L Solymar. Resonant frequencies of a combination of split rings: Experimental, analytical and numerical study. *Microwave and optical technology letters*, 46(5):473–476, 2005.

[37] W Reyes, E Peter, G Bolger, and C Sie. Factors influencing thin gold performance for separable connectors. *IEEE Transactions on Components, Hybrids, and Manufacturing Technology*, 4(4):499–508, 1981.

[38] LJ Rogla, J Carbonell, and VE Boria. Study of equivalent circuits for open-ring and split-ring resonators in coplanar waveguide technology. *IET microwaves, antennas & propagation*, 1(1):170–176, 2007.

[39] Hiroo Sekiya and Marian K Kazimierczuk. Design of rf-choke inductors using core geometry coefficient. In *Proc. Electrical Manufacturing and Coil Winding Conf*, 2009.

[40] Kaushik Sengupta, Tadao Nagatsuma, and Daniel M Mittleman. Terahertz integrated electronic and hybrid electronic–photonic systems. *Nature Electronics*, 1(12):622–635, 2018.

[41] Kaushik Sengupta and Xue Wu. Thz silicon systems on chip: Em-circuits-systems codesign approach. In *2017 42nd International Conference on Infrared, Millimeter, and Terahertz Waves (IRMMW-THz)*, pages 1–3. IEEE, 2017.

[42] Robert Smith and Thomas Darcie. Demonstration of a low-distortion terahertz system-on-chip using a cps waveguide on a thin membrane substrate. *Optics express*, 27(10):13653–13663, 2019.

[43] Robert Smith, Afshin Jooshesh, Jinye Zhang, and Thomas Darcie. Photoconductive generation and detection of thz-bandwidth pulses using near-field coupling to a free-space metallic slit waveguide. *Optics express*, 25(22):26492–26499, 2017.

[44] Robert Levi Smith. *Terahertz Field Enhancement by Optimized Coupling and Adiabatic Tapering*. PhD thesis, 2014.

[45] Robert Levi Smith. *Experimental evaluation of low-loss/non-dispersive terahertz waveguides*. PhD thesis, 2019.

[46] AJ Tessmer, PC Chao, KHG Duh, P Ho, MY Kao, SMJ Liu, PM Smith, JM Ballingall, AA Jabra, and TH Yu. Very high performance 0.15 mu m gate-length inalas/ingaas/inp lattice-matched hemts. In *Proceedings., IEEE/Cornell Conference on Advanced Concepts in High Speed Semiconductor Devices and Circuits,*, pages 56–63. IEEE, 1989.

[47] Fawwaz T Ulaby. Fundamentals of applied electromagnetics(1999 revised and enlarged edition)(book). *Upper Saddle River, NJ: Prentice-Hall, Inc, 1999.*, 1999.

[48] Martin Van Exter, Ch Fattinger, and D Grischkowsky. Terahertz time-domain spectroscopy of water vapor. *Optics letters*, 14(20):1128–1130, 1989.

[49] Victor Georgievich Veselago. The electrodynamics of substances with simultaneously negative values of img align= absmiddle alt= eps/img and μ. *Physics-Uspekhi*, 10(4):509–514, 1968.

[50] Markus Wächter, Michael Nagel, and Heinrich Kurz. Metallic slit waveguide for dispersion-free low-loss terahertz signal transmission. *Applied Physics Letters*, 90(6):061111, 2007.

[51] Kanglin Wang and Daniel M Mittleman. Metal wires for terahertz wave guiding. *Nature*, 432(7015):376, 2004.

[52] Shinji Yanagi, Masayuki Onuma, Jiro Kitagawa, and Yutaka Kadoya. Propagation of terahertz pulses on coplanar strip-lines on low permittivity substrates and a spectroscopy application. *Applied physics express*, 1(1):012009, 2008.

[53] Liu Yu, Liu Hao, Tang Meiqiong, Huang Jiaoqi, Liu Wei, Dong Jinying, Chen Xueping, Fu Weiling, and Zhang Yang. The medical application of terahertz technology in non-invasive detection of cells and tissues: opportunities and challenges. *RSC advances*, 9(17):9354–9363, 2019.

[54] Huan Zou, Haiyang Wang, and Pingshan Wang. On-chip tapered transmission line transformer based on coplanar waveguide. In *The 2012 International Workshop on Microwave and Millimeter Wave Circuits and System Technology*, pages 1–4. IEEE, 2012.